SANDIA REPORT
SAND2007-0992
Unlimited Release
Printed March 2007

Current Scaling of Axially Radiated Power in Dynamic Hohlraums and Dynamic Hohlraum Load Design for ZR

Tom Nash, Tom Sanford, and Ray Mock

Prepared by
Sandia National Laboratories
Albuquerque, New Mexico 87185 and Livermore, California 94550

Sandia is a multiprogram laboratory operated by Sandia Corporation,
a Lockheed Martin Company, for the United States Department of Energy's
National Nuclear Security Administration under Contract DE-AC04-94AL85000.

Issued by Sandia National Laboratories, operated for the United States Department of Energy by Sandia Corporation.

Available to DOE and DOE contractors from
U.S. Department of Energy
Office of Scientific and Technical Information
P.O. Box 62
Oak Ridge, TN 37831

Telephone: (865) 576-8401
Facsimile: (865) 576-5728
E-Mail: reports@adonis.osti.gov
Online ordering: http://www.osti.gov/bridge

Available to the public from
U.S. Department of Commerce
National Technical Information Service
5285 Port Royal Rd.
Springfield, VA 22161

Telephone: (800) 553-6847
Facsimile: (703) 605-6900
E-Mail: orders@ntis.fedworld.gov
Online order: http://www.ntis.gov/help/ordermethods.asp?loc=7-4-0#online

SAND2007-0992
Unlimited Release
Printed March 2007

Current Scaling of Axially Radiated Power in Dynamic Hohlraums and Dynamic Hohlraum Load Design for ZR

Tom Nash, Tom Sanford, and Ray Mock
Sandia National Laboratories
Albuquerque NM 87185

ABSTRACT

We present designs for dynamic hohlraum z-pinch loads on the 28 MA, 140 ns driver ZR. The scaling of axially radiated power with current in dynamic hohlraums is reviewed. With adequate stability on ZR this scaling indicates that 30 TW of axially radiated power should be possible. The performance of the dynamic hohlraum load on the 20 MA, 100 ns driver Z is extensively reviewed. The baseline z-pinch load on Z is a nested tungsten wire array imploding onto on-axis foam. Data from a variety of x-ray diagnostics fielded on Z are presented. These diagnostics include x-ray diodes, bolometers, fast x-ray imaging cameras, and crystal spectrometers. Analysis of these data indicates that the peak dynamic radiation temperature on Z is between 250 and 300 eV from a diameter less than 1 mm. Radiation from the dynamic hohlraum itself or from a radiatively driven pellet within the dynamic hohlraum has been used to probe a variety of matter associated with the dynamic hohlraum: the tungsten z-pinch itself, tungsten sliding across the end-on apertures, a titanium foil over the end aperture, and a silicon aerogel end cap. Data showing the existence of asymmetry in radiation emanating from the two ends of the dynamic hohlraum is presented, along with data showing load configurations that mitigate this asymmetry. 1D simulations of the dynamic hohlraum implosion are presented and compared to experimental data. The simulations provide insight into the dynamic hohlraum behavior but are not necessarily a reliable design tool because of the inherently 3D behavior of the imploding nested tungsten wire arrays.

CONTENTS

FIGURES

TABLES

INTRODUCTION

Z was a 20 MA current-driver with a 100 ns rise time built to implode z-pinches for research in the areas of weapons physics, weapons effects, and inertial confinement fusion (ICF). [1]

One type of z-pinch with application to both weapons physics and ICF is the dynamic hohlraum. [2-6] This z-pinch was usually configured on Z as nested tungsten wire arrays of 240 and 120 7.5 μm diameter wires positioned at diameters of 40 and 20 mm. The nested tungsten wire arrays imploded onto an on-axis foam 5 mm in diameter. On Z the dynamic hohlraum was 1 cm long, the tungsten wire arrays weighed 2 and 1 mg, the foam mass was 3 mg, and the foam density was 0.014 g/cc.

In the dynamic hohlraum the imploding tungsten z-pinch launches a radiating shock wave in the foam and also traps that radiation. On Z the peak radiation temperature averaged over a 2.4 mm diameter exit aperture was 230 eV.

Before its development on SATURN and on Z, several authors had already proposed the dynamic hohlraum or flying radiation case as a radiation source. [7,8] The dynamic hohlraum became practical through the improved z-pinch performance by using large number wire-arrays on SATURN. [9] Placing on-axis foam inside the large wire-number array on SATURN gave a stable dynamic hohlraum. [10]

Because of the larger implosion time on Z as compared to SATURN a nested wire-array was used on Z to further stabilize the pinch implosion. [11] The dynamic hohlraum source has been used on Z for high temperature radiation flow experiments. [8,11]

It is the purpose of this report to design dynamic hohlraum loads for the 28 MA, 140 ns upgrade to Z we designate as ZR. To this end we review dynamic hohlraum experimental data in Section II. Simulation results and current scaling are presented in Section III. Dynamic hohlraum loads proposed for ZR are presented in Section IV.

II. EXPERIMENTAL DATA

Early successful dynamic hohlraum experimental results from SATURN are depicted in Figure 1 showing 1 ns resolved x-ray images of the single tungsten wire-array z-pinch as it imploded onto an aerogel foam. SATURN drove 7 MA into a z-pinch imploding in 50 ns. The tungsten wire array was composed of 120 wires on a 17.5 mm diameter weighing 450 μg/cm. The silicon aerogel foam was 4 mm in diameter and weighed 650 μg/cm. The pinch was 2 cm long.

The x-ray images of Figure 1 used a view from the side of the z-pinch. Gating times for the x-ray images relative to the power radiated to the side are depicted in the Figure 1 inset. From the image in Figure 1 designated as frame 5 one sees that the on-axis foam has been compressed by the z-pinch to a diameter less than 1 mm.

In these early experiments on SATURN the only end-on diagnostics fielded were x-ray diodes (XRDs). Based on the response of these XRDs used from both the end and the side the radiation temperature on SATURN dynamic hohlraum was estimated to reach 150 eV with significant radiation trapping at photon energies less than 500 eV.

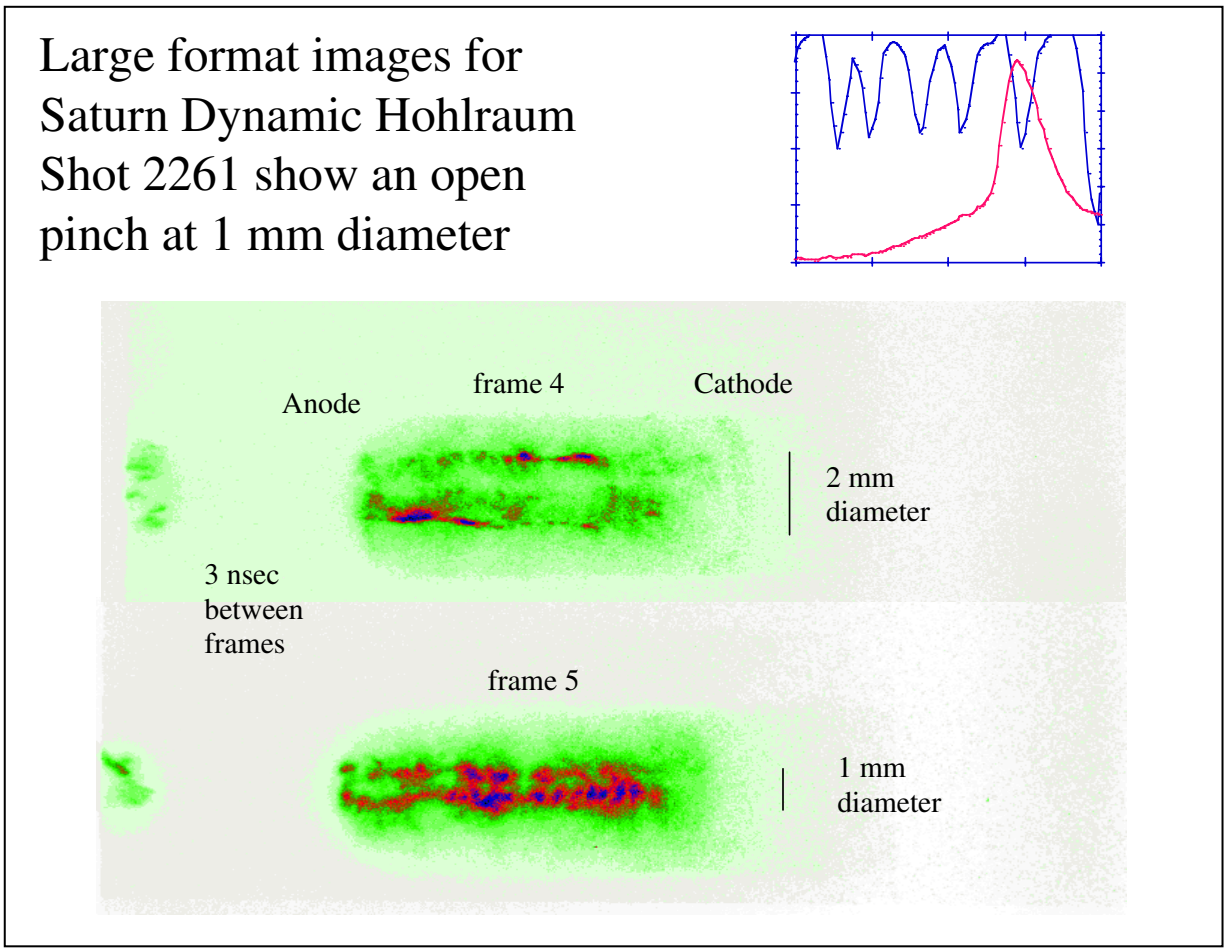

Figure 1. Gated side-on dynamic hohlraum x-ray images from SATURN.

To scale the dynamic hohlraum load from SATURN to Z we kept the 0D simulated implosion velocity similar on the two machines at just over 60 cm/μs. Since Z requires twice the implosion time of SATURN to reach peak current we doubled the diameter of the pinch load on Z relative to SATURN. This doubling of the implosion time on Z with respect to SATURN gave cause for concern on Z regarding the growth of z-pinch instabilities over longer duration implosion times.

In an effort to reduce the effects of the growth of the Rayleigh-Taylor instability on Z the nested wire array was introduced. [10] At the time of the implementation of the innovation of nesting the tungsten wire arrays it was thought that the individual wires merged into a plasma shell and that the collision of the two nests during the implosion was hydrodynamic. Since that time experiments have been performed to conclude that the outer array implodes past the inner array in a transparent mode with minimal interaction between the two arrays as they collide. After the collision of the two nests, the current switches to the inner array. [12, 13] The stability of the pinch is therefore dictated by the time scale of the implosion of the inner array, 25 ns on Z, rather than the longer implosion time of the outer array, 100 ns, on Z. This issue will continue to be of concern in scaling from Z to the 140 ns implosion times of ZR.

The standard load for the dynamic hohlraum on Z is depicted in Figure 2. It consisted of nested tungsten wire-arrays at 4 and 2 cm diameter with 240 and 120 7.5 μm diameter wires weighing 2 and 1 mg/cm. The foam target had a 5 mm diameter, 0.014 g/cc density, and weighed 3 mg/cm. Typically the load was 1 cm long. In Figure 2 the current return can at 5 cm diameter was solid with only an axial viewing aperture. More typically the return can on Z had 18 side-on viewing slots for side-on diagnostics.

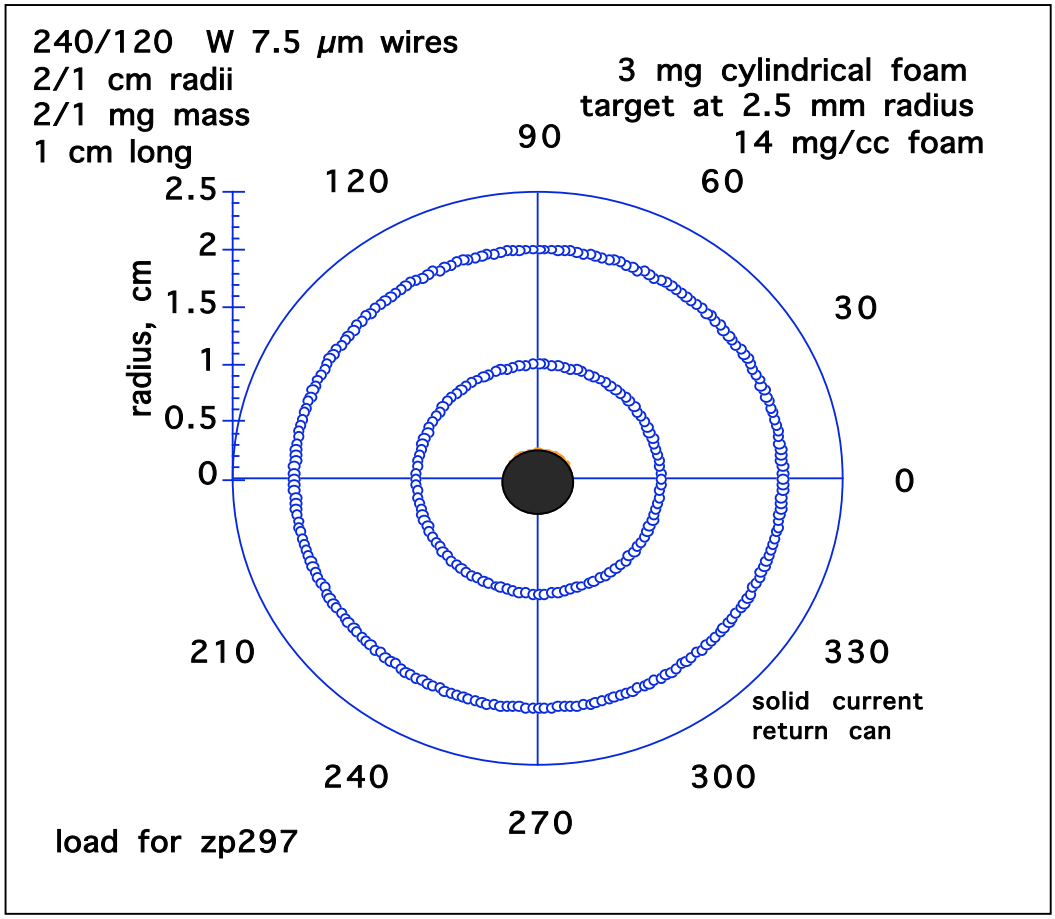

Figure 2. Dynamic hohlraum load for Z.

The load current and power radiated to the side for the load of Figure 2 on Z is shown in Figure 3. The peak current is just over 21 MA and the implosion time to the peak of power radiated to the side is 112 ns. Side radiated power is 140 TW with a 3 ns fwhm.

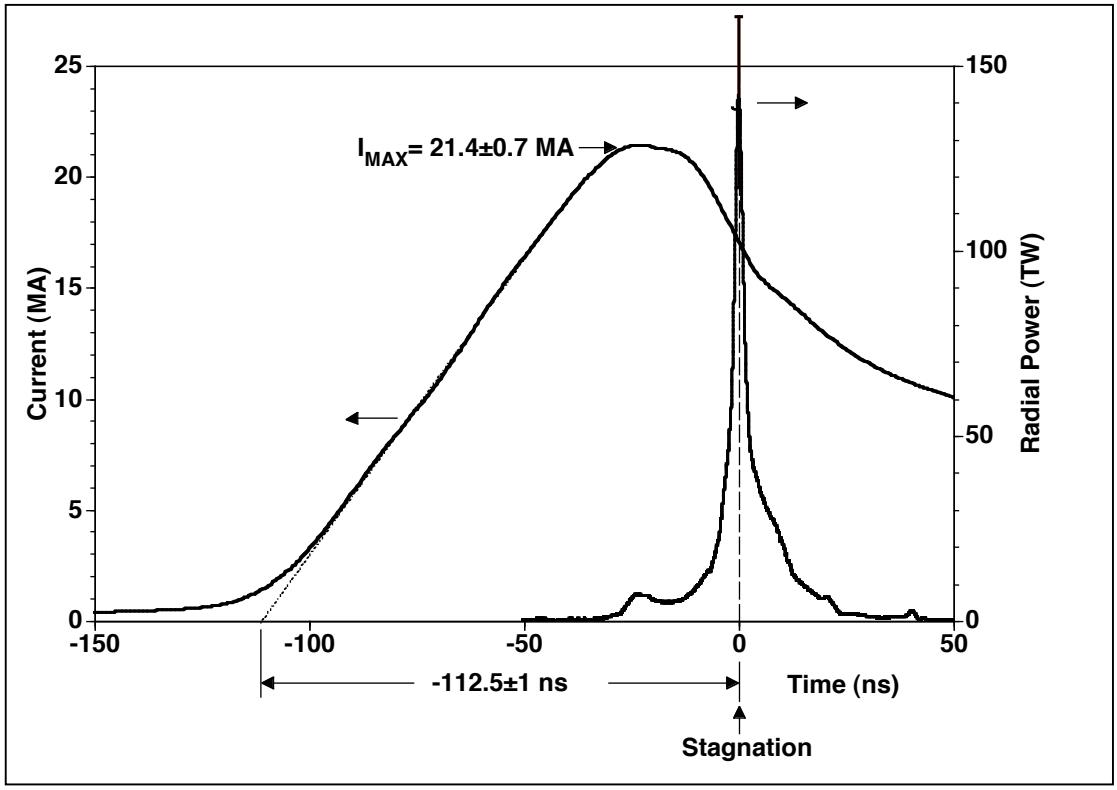

Figure 3. Load current and power radiated to the side for the dynamic hohlraum on Z.

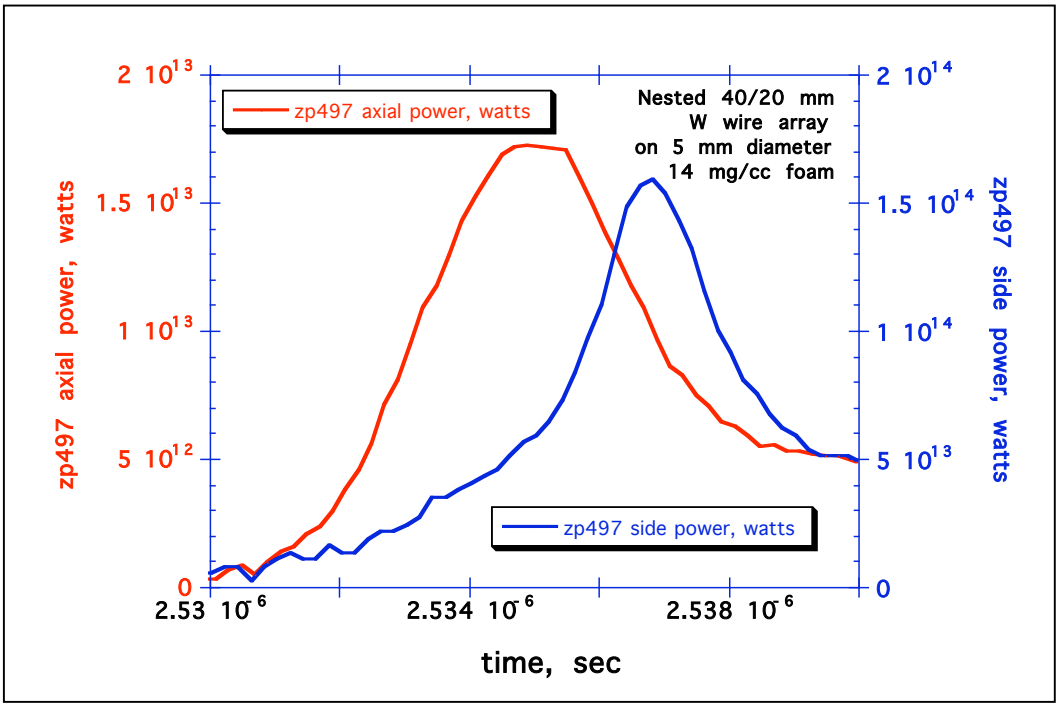

Figure 4. Axially and radially radiated power in dynamic hohlraum on Z.

In Figure 4 we present axially radiated power plotted along with power radiated to the side as recorded on Z shot 497. The radiated power was measured by normalizing an XRD trace with yield determined by bolometers. On this shot the axial power reached 17 TW and the power to the side reached 160 TW. The power out the axis peaks 2.5 ns before the power radiated to the side. Also the axial power is falling as the radial power is rising at 536 ns in Figure 4. The inflection point in the rise of the side power at 2535.5 ns in Figure 4 happens when the imploding shock wave in the foam has reflected back and impacted the incoming tungsten pinch material.

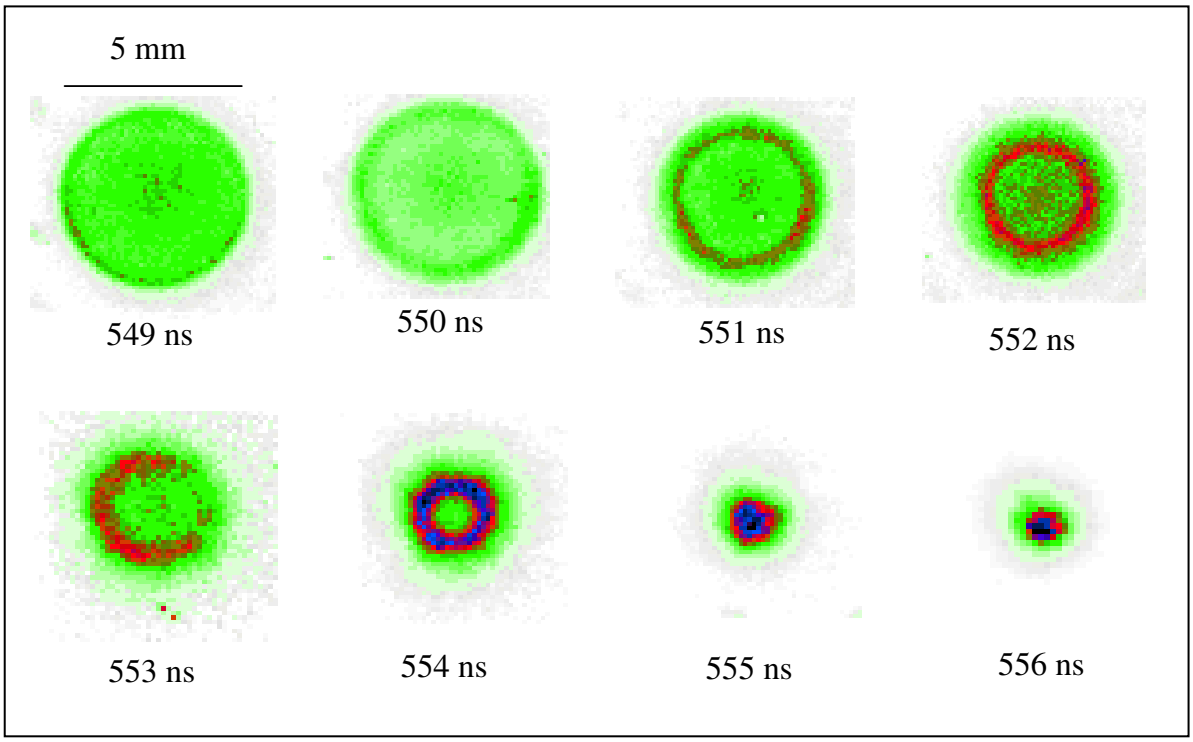

Figure 5. On-axis time-resolved x-ray images of the converging radiating shock wave in the dynamic hohlraum as recorded on Z shot 670.

An on-axis time-resolved pinhole camera has imaged the converging radiating shock wave and these images are presented in Figure 5 for Z shot 670. The on-axis viewing aperture is 5 mm in diameter. The shock wave converges towards the axis at a velocity of 35 cm/μs.

Using the measured axially radiating power and measuring the relative timing of the XRDs and the on-axis time-resolved pinhole camera it is possible to convert the images of Figure 5 into the units of radiation temperature. [14] This conversion is shown in Figures 6 and 7. These figures plot azimuthally averaged radiation temperatures as a function of radius parametric in time. In Figure 6 the small humps on axis are due to background noise from Bremsstrahlung radiation. [15] During most of its convergence the radiation temperature of the shock wave is less than 200 eV. When the converging shock wave reaches the axis its radiation temperature peaks at 300 eV with a radial extent less than 1 mm.

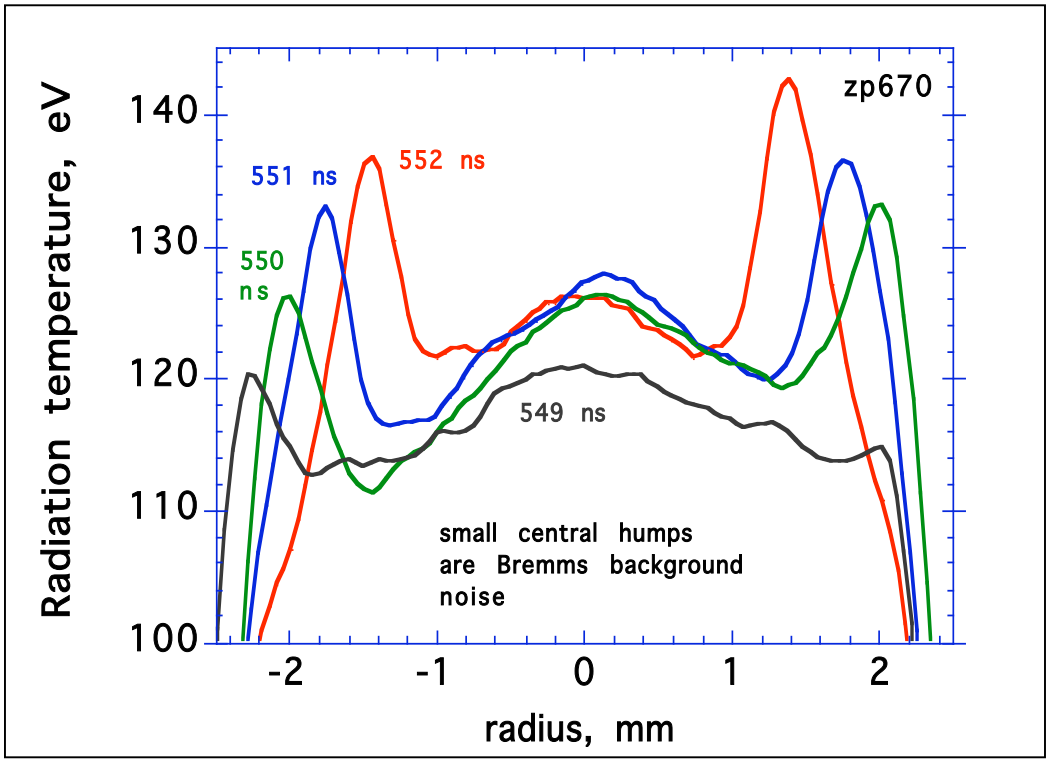

Figure 6. Radial lineouts of radiation temperature of dynamic hohlraum for Z shot 670.

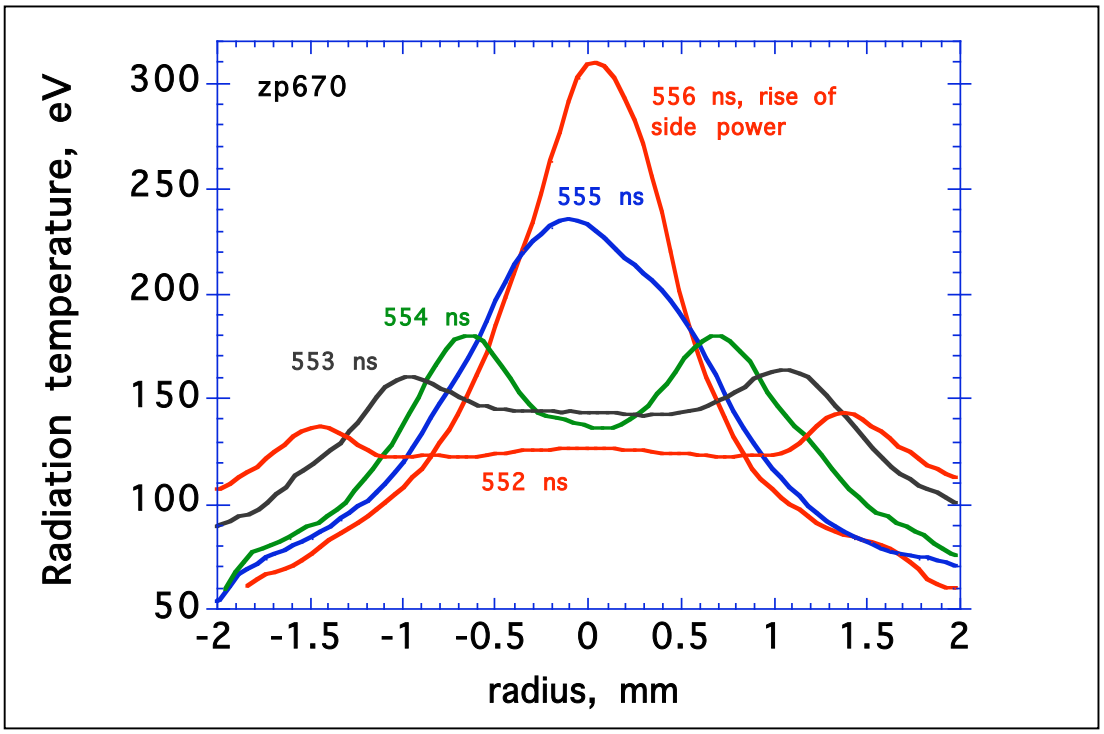

Figure 7. Radial lineouts of radiation temperature of dynamic hohlraum for Z shot 670.

Figures 5 through 7 show images and radiation temperature of the converging shock wave in the foam but do not obviously show the radiation temperature or location of the tungsten z-pinch material that constitutes the radiation case. In experiments designed and lead by Gordon Chandler the location and radiation temperature of the tungsten case material was measured. An on-axis time-resolved x-ray image depicting the relative locations of the radiating shock wave in the foam and the trailing tungsten radiation case is shown in Figure 8 as recorded on Z shot 799. In this shot a beryllium strip was placed at a depth of 3.75 mm into the foam to provide contrast between the converging shock wave and trailing tungsten. As designed when viewed along the axis the tungsten is much more optically thick than the radiating shock wave. The beryllium is absorbing to the shock wave but has little impact on the image of the tungsten which itself is thick over a 3.75 mm depth.

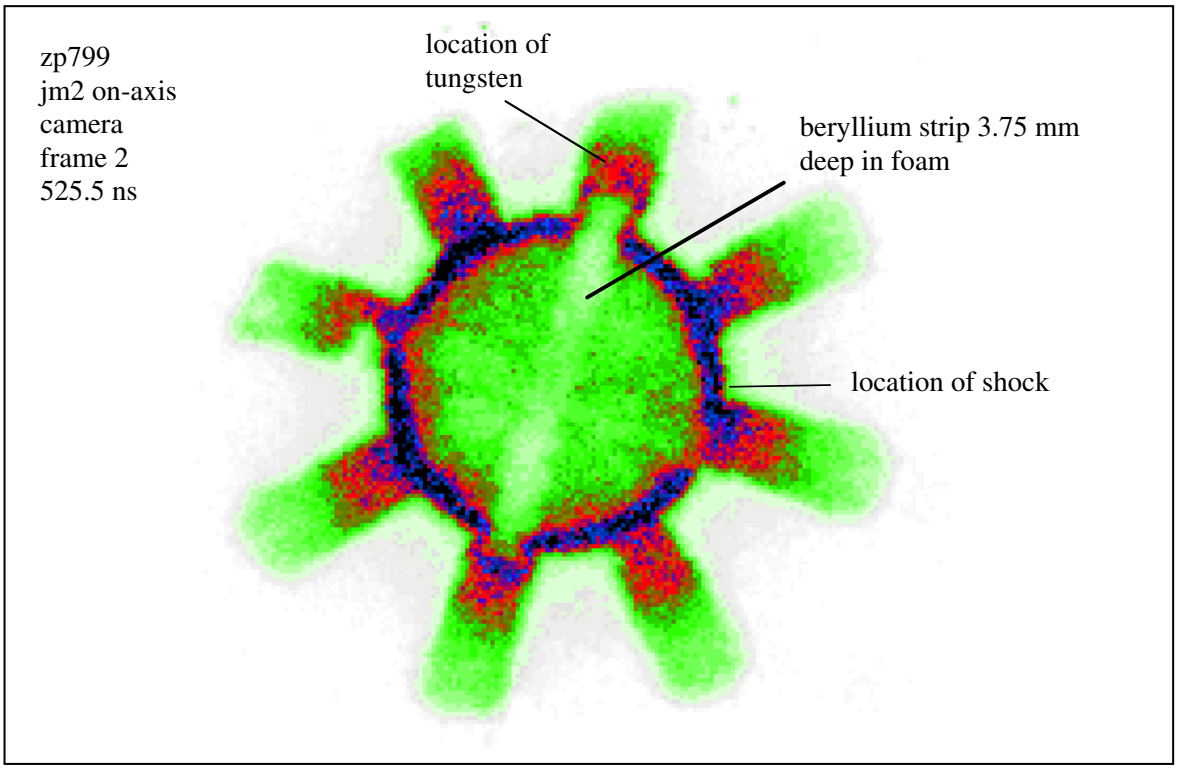

Figure 8. On-axis time-resolved x-ray image recording the relative location and emission of the radiating shock wave and the tungsten radiation case.

Lineouts of time-resolved x-ray images from Z shot 799 taken along and off the beryllium strip are shown in Figures 9 and 10. The solid lineouts are taken along the beryllium strip and their peaks give the location of the tungsten. The dashed lineouts are taken off the beryllium strip and their peaks give the location of the radiating shock wave. During the early time frames when this data was recorded, several ns before shock stagnation; the tungsten is trailing the shock wave by roughly 1 mm and is very roughly 15% cooler in radiation temperature. At later times as the temperature of the radiating shock wave increases the contrast between the tungsten and shock wave location provided by the beryllium strip is lost, possibly due to the beryllium becoming transparent at higher temperatures.

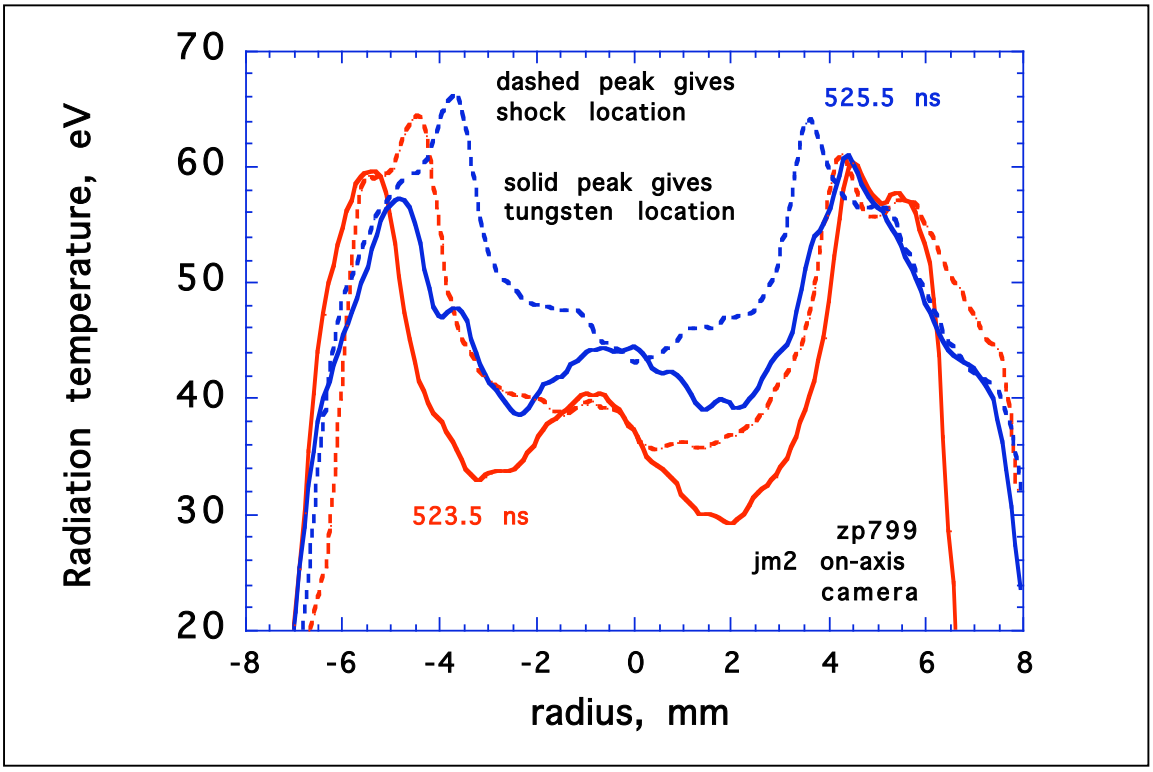

Figure 9. Lineouts of on-axis time-resolved x-ray images showing the relative locations and radiation temperatures of the shock wave and the trailing tungsten case.

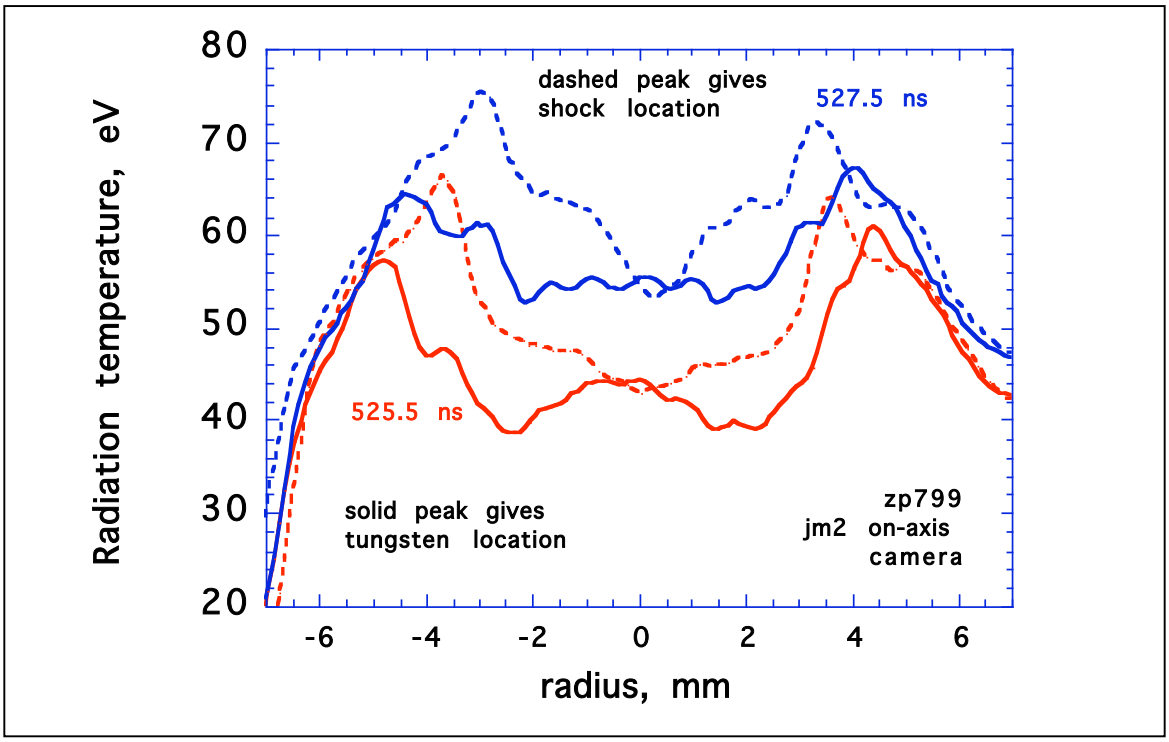

Figure 10. Lineouts of on-axis time-resolved x-ray images showing the relative locations and radiation temperatures of the shock wave and the trailing tungsten case.

Radiation from within the dynamic hohlraum may be used to probe matter near the dynamic hohlraum including the hohlraum wall itself.

Several Z shots have been taken with an inertial confinement fusion (ICF) pellet placed inside the dynamic hohlraum. The implosion of this pellet driven by the dynamic hohlraum radiation typically produced a small 200 μm diameter hot spot with a radiation temperature of approximately 450 eV. [16] The spectrum from this hot spot as recorded on Z shot 1031 by end-on and side-on time and space resolved elliptical crystal spectrometers is shown in Figure 11. Jim Bailey and Greg Rochau developed these instruments. The spectral response of the instrument was taken from Henke. [17] The recorded spectra were normalized with photoconducting detectors fielded on the end and side of the dynamic hohlraum. In Figure 11 the pellet hot spot spectrum viewed axially is much brighter than that recorded from the side due to the absorption of the pellet hot spot radiation by the tungsten wall of the dynamic hohlraum. By taking the natural logarithm of the ratio of the two spectra in Figure 11 we measure a tungsten wall optical depth of 3.4 between 3 and 4 keV at the time of the hot spot radiation burst, a few ns before the stagnation of the radiating shock wave. Thus the imploding ICF pellet has served as a diagnostic tool to measure the optical depth of the tungsten wall in the dynamic hohlraum. The spectral lines in Figure 11 are from argon used as a tracer impurity in the ICF pellet.

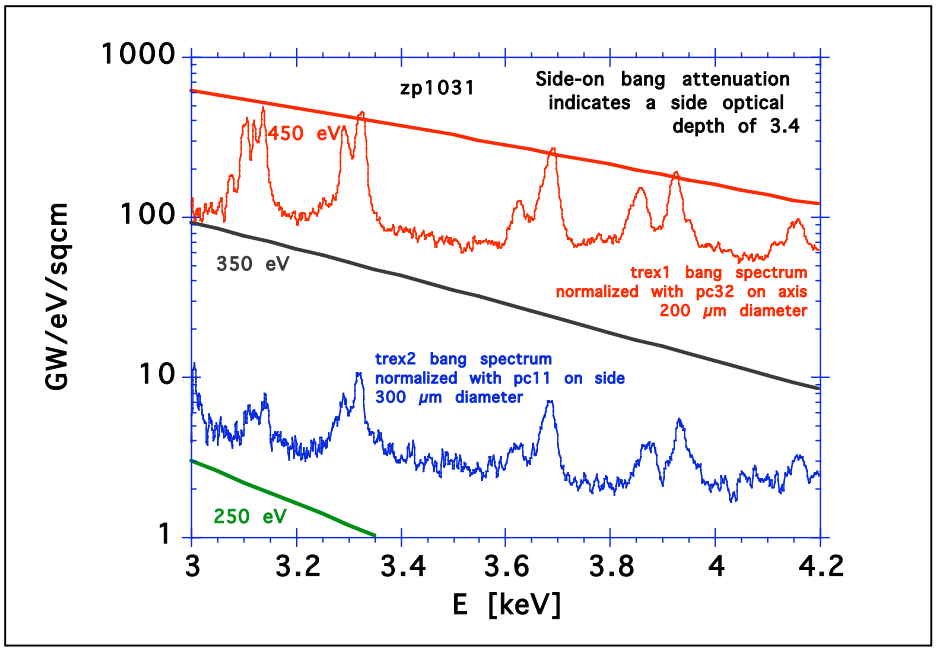

Figure 11. ICF pellet hot spot spectra recorded end-on and side-on with space and time resolved elliptical crystal spectrometers.

The ICF pellet hot spot radiation burst has also been used to probe the conditions of foils and foams placed on axis atop the dynamic hohlraum foam.

In Figure 12 we present data on Z shot 960 from a spatially resolved temporally integrated crystal spectrometer fielded on axis viewing the dynamic hohlraum through a titanium filter. The titanium filter was fielded to improve the symmetry of the radiation field applied to an ICF pellet. The temporal width of the hot spot radiation burst and the

radiation burst from the shock stagnation are measured with PCDs. The crystal instrument itself spatially resolves the pellet hot spot from the shock stagnation by being fielded at an angle of 9 degrees with respect to the axis. As shown in Figure 12 the pellet hot spot has a radiation temperature of 450 eV while the radiation temperature of the shock stagnation is 300 eV. Titanium 1 to 2 and 1 to 3 absorption lines from L-shell ionization states appear in both of these spectra near 4.5 and 5 keV. At the time of the pellet hot spot burst, several ns before the shock stagnation, the titanium absorption lines are from lower ionization states. At the time of the shock stagnation, the ionization level of the titanium end foil has increased indicating that it has been heated as the temperature of the dynamic hohlraum has been increasing.

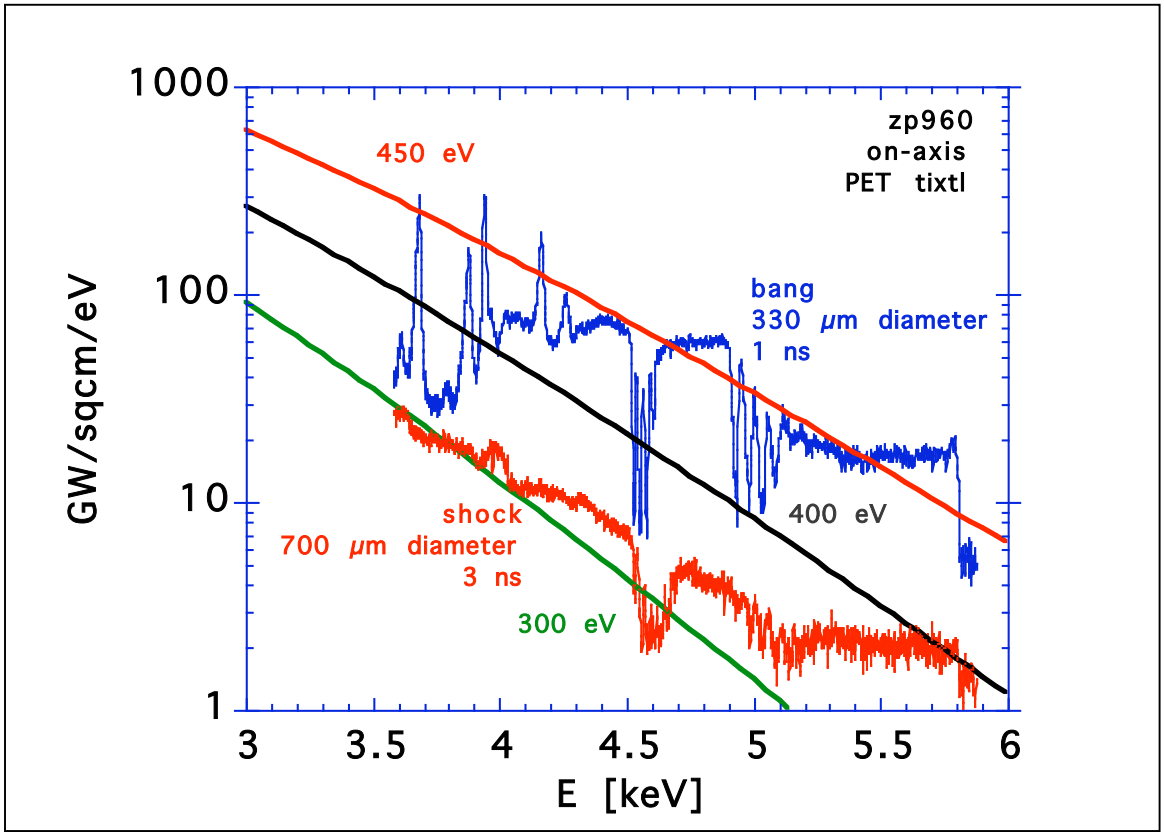

Figure 12. Pellet hot spot and shock stagnation spectra showing absorption lines from a titanium end foil.

The impact of the choice of material for the dynamic hohlraum wire-array is shown in Figure 13. This figure presents the axially radiated power for wire-arrays composed of tungsten, titanium, and nickel-clad titanium. The motivation of this study was to use a pinch material much more transparent to argon tracer lines above 3 keV but only modestly more transparent to dynamic hohlraum radiation largely under 1 keV, and thereby enable side-on diagnosis of the pellet hot spot. As is shown in Figure 13 the nickel-clad titanium wire-array gives a 20% power reduction along the axis compared to a tungsten wire-array. A pure titanium wire-array gives a further 30% reduction.

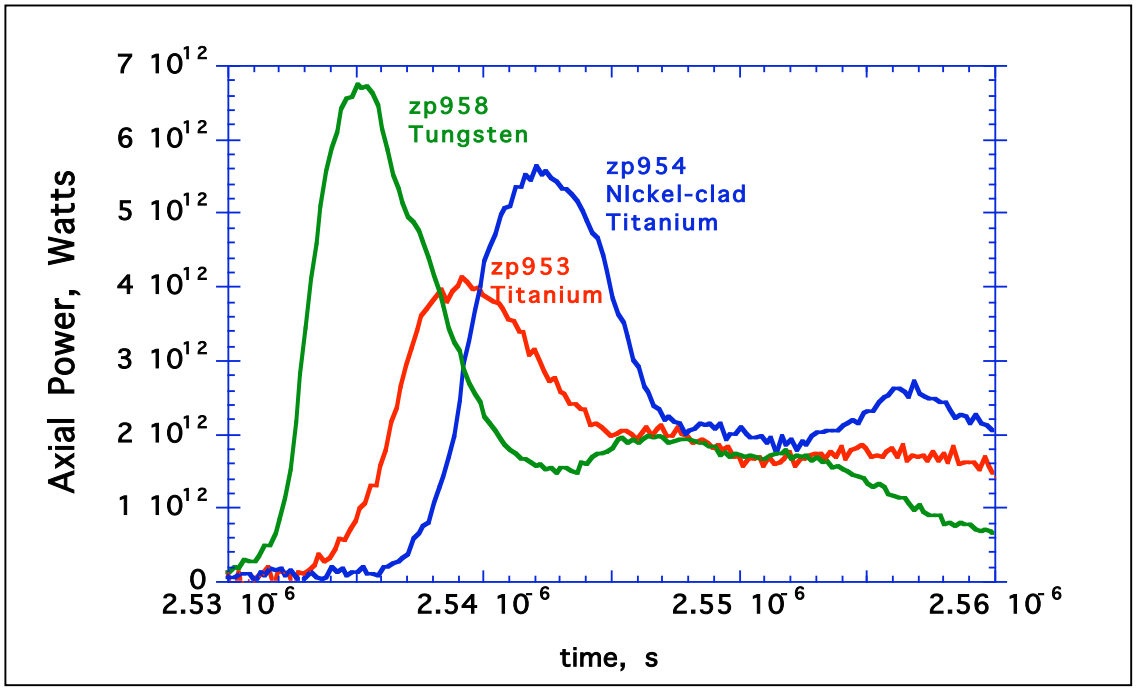

Figure 13. Axially radiated power for tungsten, nickel-clad titanium, and titanium wire-arrays.

In experiments conducted by the LANL weapons physics team a silicon aerogel foam was placed atop the dynamic hohlraum foam. Figure 14 presents the spectrum obtained from an on-axis spatially resolved crystal spectrometer viewing the dynamic hohlraum through the aerogel foam on Z shot 991. [18] The spectrum was normalized with an on-axis PCD. The 250 eV radiation temperature of the shock stagnation is modified by absorption by He-like silicon lines and by the ionization edge of He-like silicon near 2400 eV. The silicon absorption spectrum is magnified in Figure 15 and compared to a simulated spectrum produced from a 250 eV blackbody backlighting aerogel foam in LTE at 150 eV. This comparison indicates that in this configuration the dynamic hohlraum radiation has heated the aerogel foam to 150 eV at the time of shock stagnation.

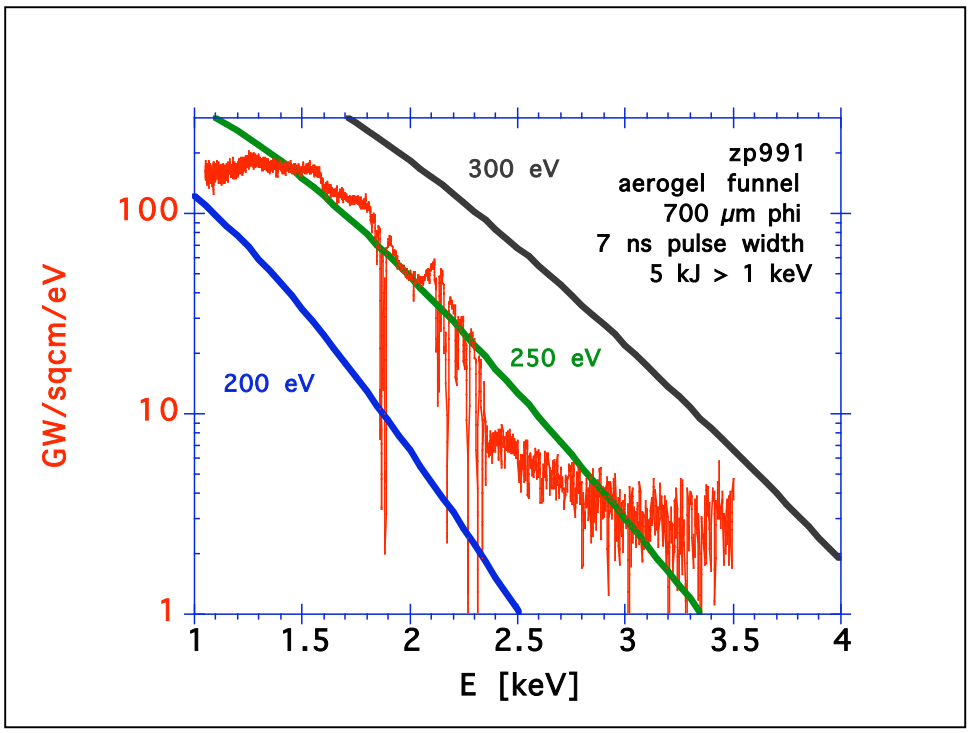

Figure 14. Spectrum from the shock stagnation backlighting a silicon aerogel foam.

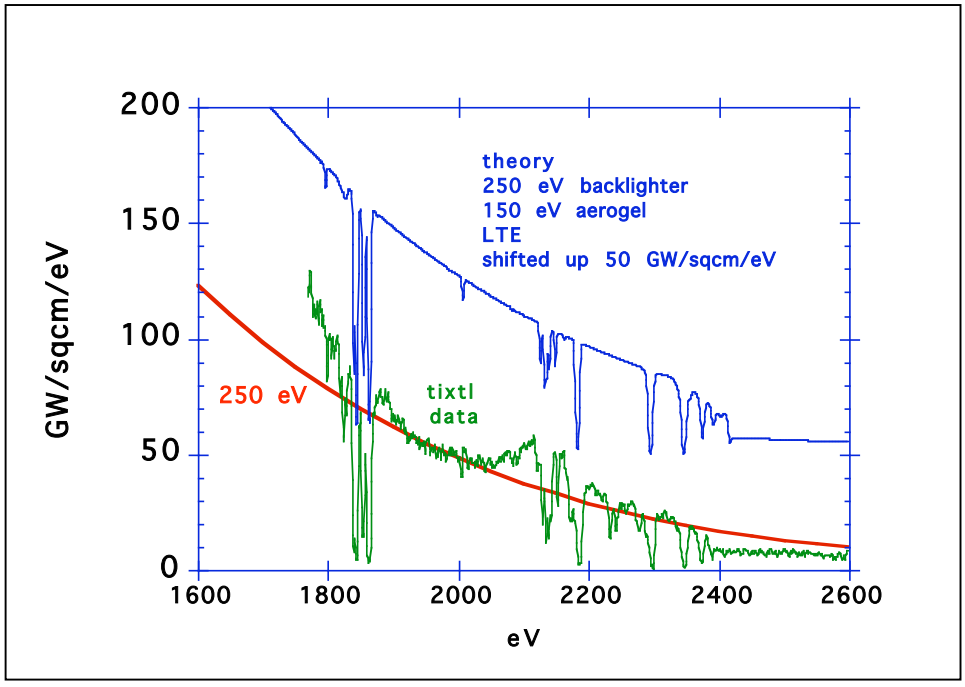

Figure 15. Comparison of measured to simulated spectrum for the dynamic hohlraum shock stagnation radiation backlighting silicon aerogel foam.

The spectrum from the silicon aerogel foam was also recorded with a spatially integrating temporally resolving crystal spectrometer. Figure 16 shows a color image of four time gates recorded with this instrument. The timing is called out with respect to the time of the shock stagnation. Silicon absorption lines are seen against the continuum radiation of the shock stagnation. As time proceeds, the dynamic hohlraum radiation as a backlighter diminishes, and the aerogel foam heats as evidenced by emission from H-like silicon. Also at +4 ns and later the lines in emission are blue shifted from their initial position in absorption.

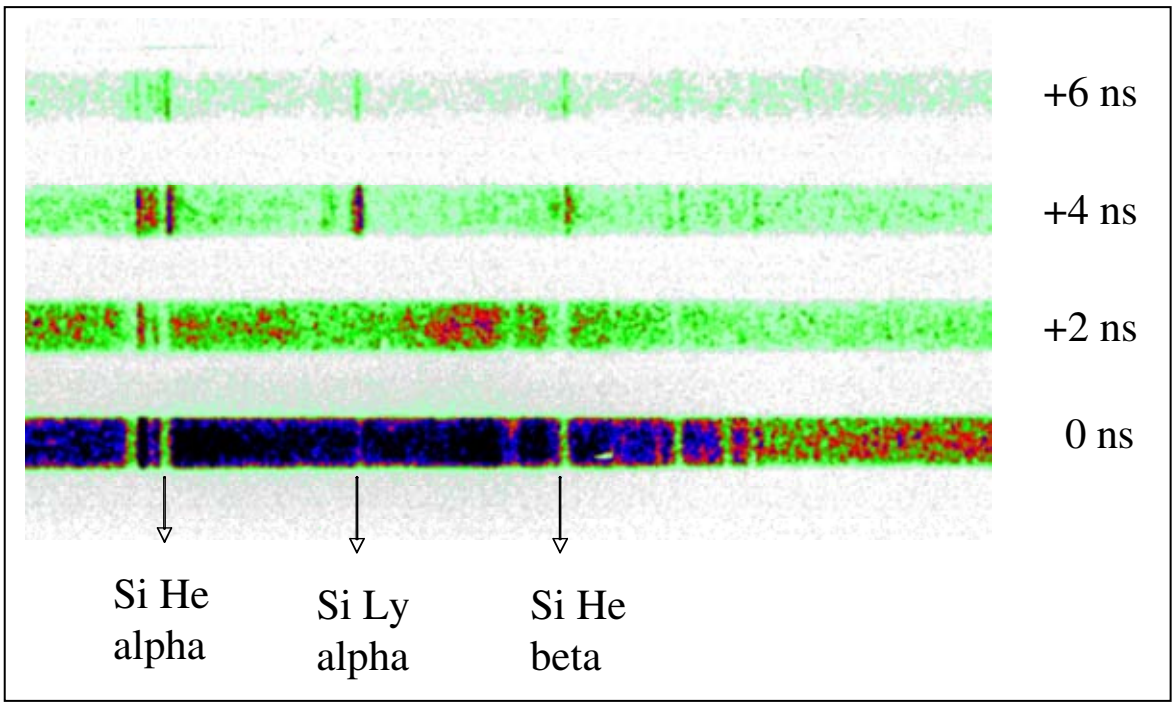

Figure 16. Data from an on-axis time resolved crystal spectrometer showing silicon absorption and emission lines from a silicon aerogel foam atop the dynamic hohlraum.

The blue shift of the silicon Lyman alpha line was recorded with high resolution by an end-on time-integrated crystal spectrometer in 4th order. The high resolution enabled measurement of the individual fine structure components of the Lyman alpha line in absorption as shown in Figure 17. The emission component is blue shifted likely due to the jetting of the aerogel end cap induced by the high pressure of the dynamic hohlraum stagnation. The shift from the center of the fine structure components in absorption to the peak of the emission feature is 3.1 eV and this value implies a jetting velocity of 46 cm/μs. The fine structure components are not resolved in emission, likely due to a distribution of jetting velocity within the aerogel.

The dynamic hohlraum radiation may also serve as a probe of imploding tungsten that crosses over the ends of the radiation cavity. Figure 18 shows spectra recorded with time-integrated crystal spectrometers fielded both above and below the dynamic hohlraum. The data from the bottom spectrometer shows a pronounced tungsten M-shell absorption feature that is much weaker in the data from the top spectrometer. The power radiated out the top of the dynamic hohlraum on Z for the standard load is up to twice that radiated out the bottom as illustrated in Figure 19. [19] The same tungsten producing the absorption feature at 2 keV

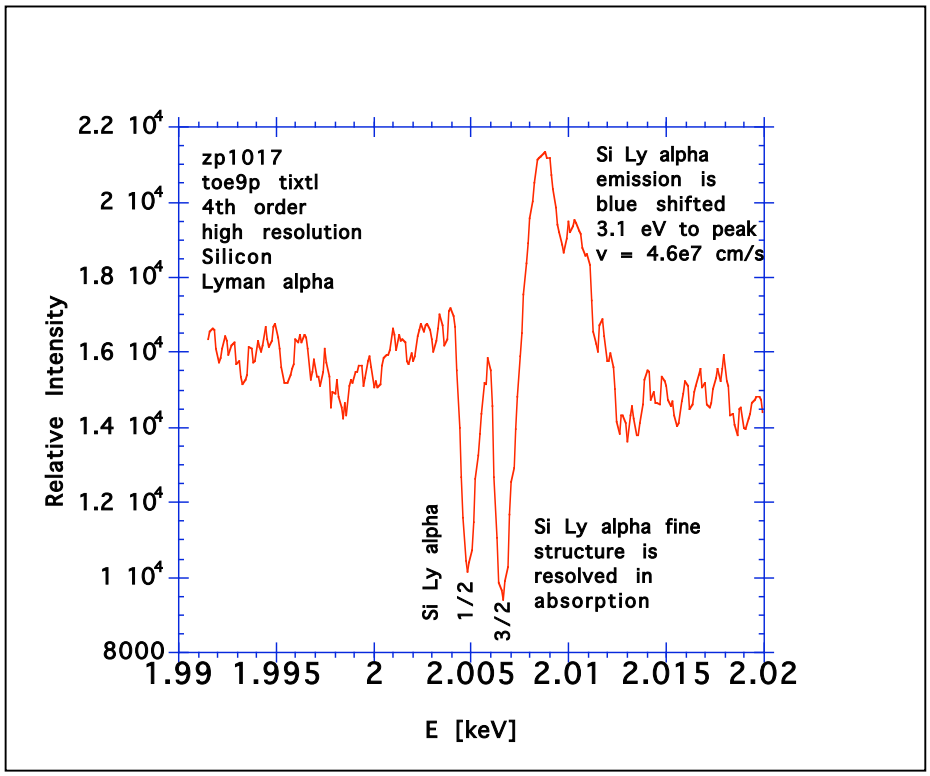

Figure 17. Silicon Lyman alpha line structure recorded in high resolution in 4th order.

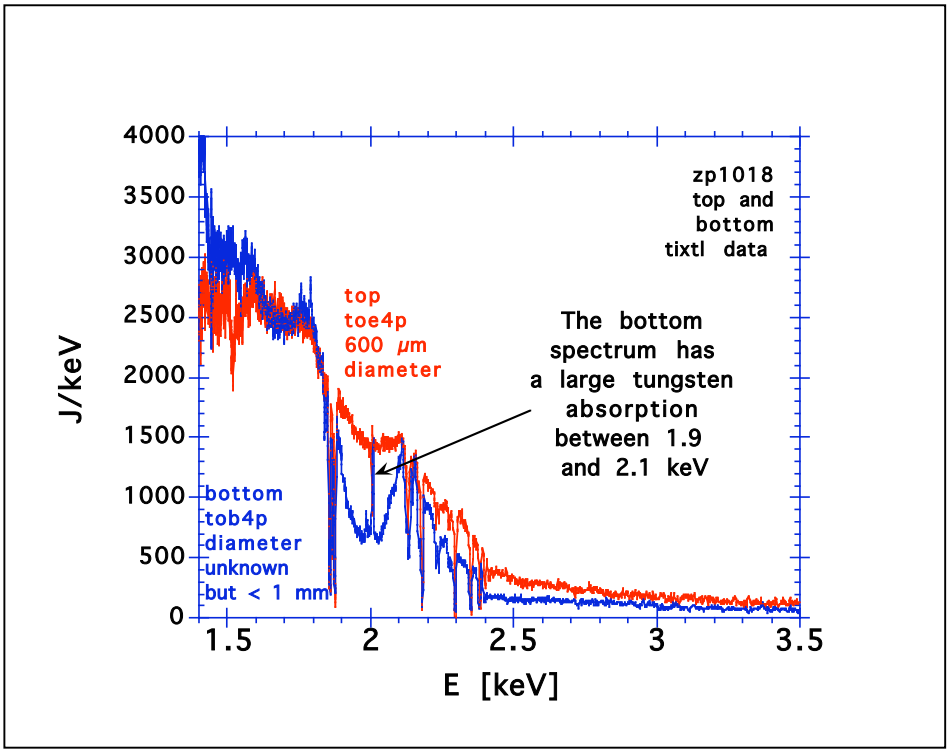

Figure 18. A tungsten spectral absorption feature is much more pronounced when viewed from the bottom of the dynamic hohlraum cavity.

in Figure 18 would also attenuate the bulk of the dynamic hohlraum radiation at energies below 1 keV. Figure 19 shows power radiated to the top and to the bottom for Z shot 1023. Although the energies radiated to the top and bottom are similar, the power radiated to the top is much greater than that radiated to the bottom. A likely explanation for this is that tungsten obscures the escape of radiation out the bottom. The lower insets of Figure 19 show time resolved crystal spectra for the top and the bottom for Z shot 1023 recorded near peak radiated power. The spectrum out the top is nearly Planckian while that out the bottom is modulated by tungsten absorption and emission features.

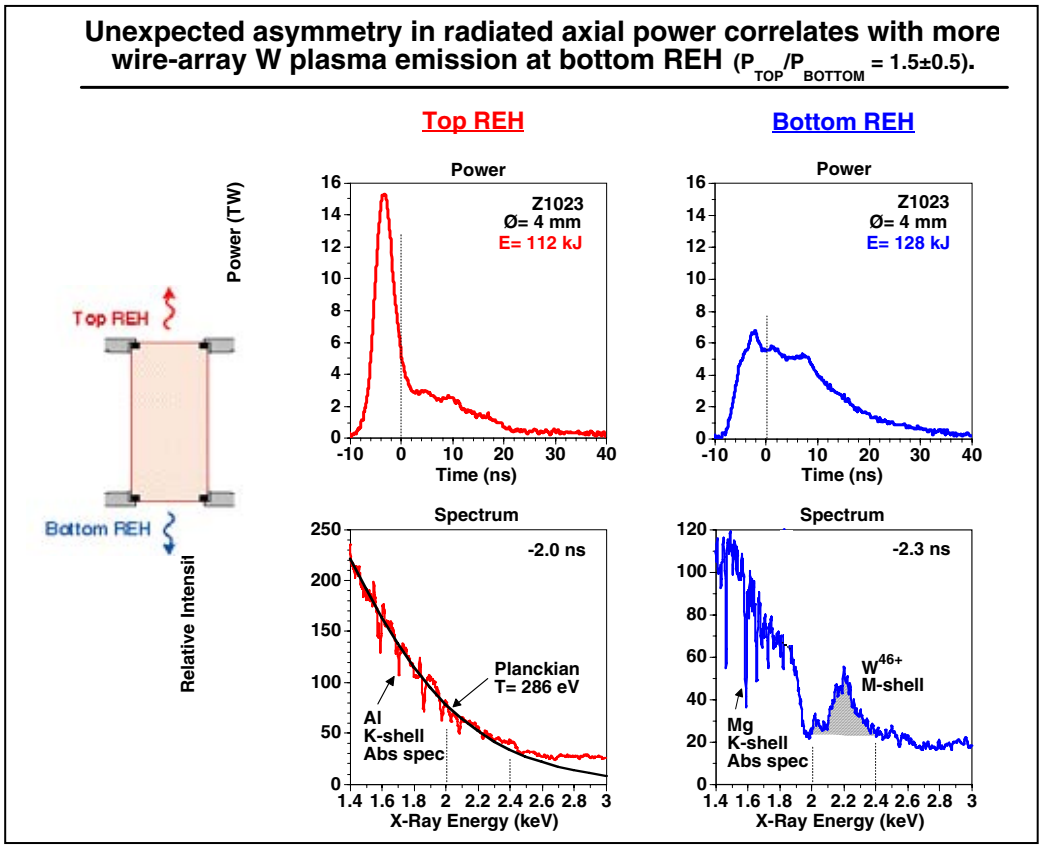

Figure 19. Up/down power asymmetry is due to tungsten obscuring bottom radiation.

Using tungsten opacities calculated by Joe MacFarlane at the University of Wisconsin it is possible to simulate the measured tungsten spectrum. This simulation is depicted in red in Figure 20. In this simple model a 250 eV blackbody source backlights tungsten plasma at 175 eV. Very little tungsten is required to attenuate the blackbody radiation. In order to simulate the tungsten emission feature at 2.2 keV there must be hotter tungsten, 390 eV in Figure 20, to produce emission at levels above the 250 eV blackbody intensity. This hotter tungsten may be from tungsten stagnating on axis at the end of the dynamic hohlraum. The cooler attenuating tungsten at 175 eV causes the tungsten absorption feature at 2 keV and also would cause attenuation of the bulk radiation below 1 keV as illustrated by the red curve in Figure 20. We strongly conclude that tungsten along the bottom of the dynamic hohlraum is responsible for the up/down power asymmetry.

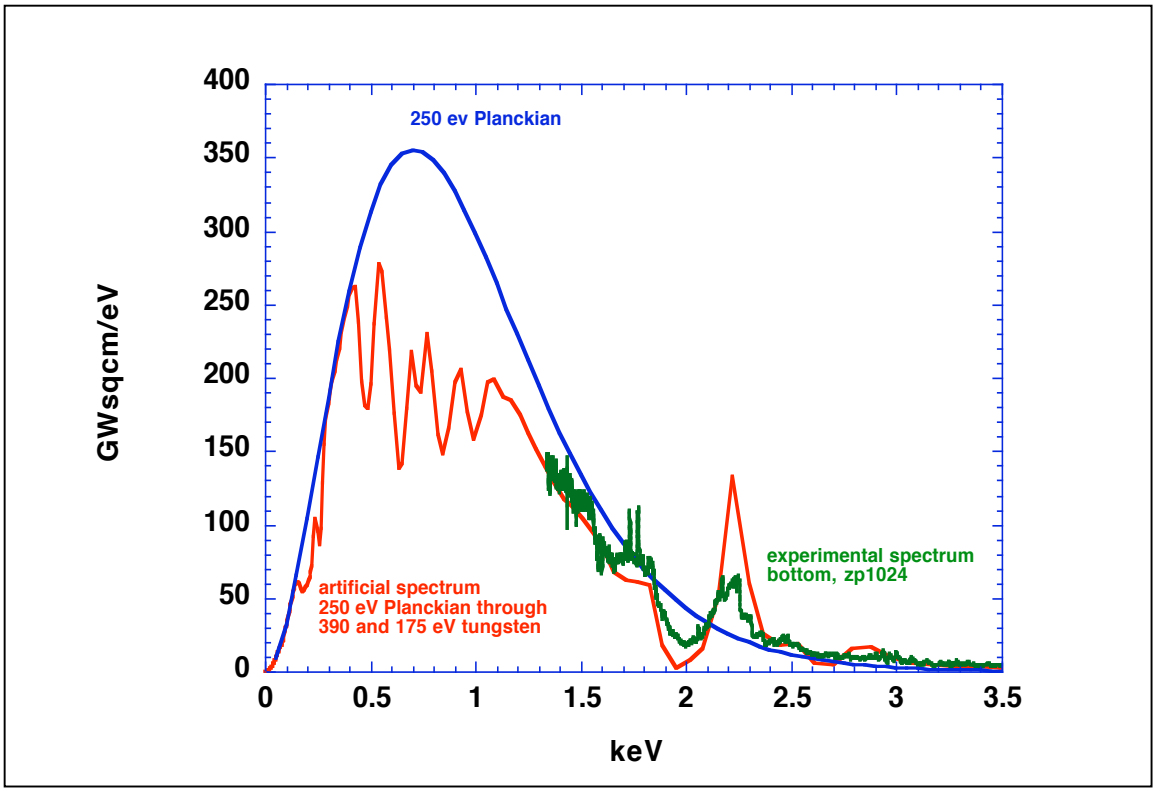

Figure 20. Measured (green) and simulated (red) dynamic hohlraum spectra including the effects of tungsten end plasma.

In an effort to eliminate the up/down power asymmetry the dynamic hohlraum foam was mounted into pedestals 3 mm in length on both the top and the bottom. The idea was for the pedestals to clip any tungsten trying to run ahead of the pinch on the ends. As shown in Figure 21 the pedestals did remove the up/down asymmetry for the standard dynamic hohlraum load on Z shot 1132. Also plotted in Figure 21 is the relative fraction of tungsten emission between 2.2 and 2.4 keV to the total continuum emission above 1.4 keV. This fraction provides an estimate of the amount of tungsten obscuring the radiation emission apertures either above or below the dynamic hohlraum. A larger fraction of tungsten spectral features correlates with greater up/down power asymmetry.

In an effort to increase the axially radiated power several scans were performed on Z. Among these were a mass scan of the imploding tungsten, a scan of the pinch length and a fixed implosion time scan of the pinch radius. The mass scan showed axially radiated power to decrease with tungsten mass increasing above 3 mg in the standard load. This result was contrary to 1D simulations. [20] The length scan showed the axially radiated power scales inversely with the pinch length down to a length of 7.5 mm. [21]

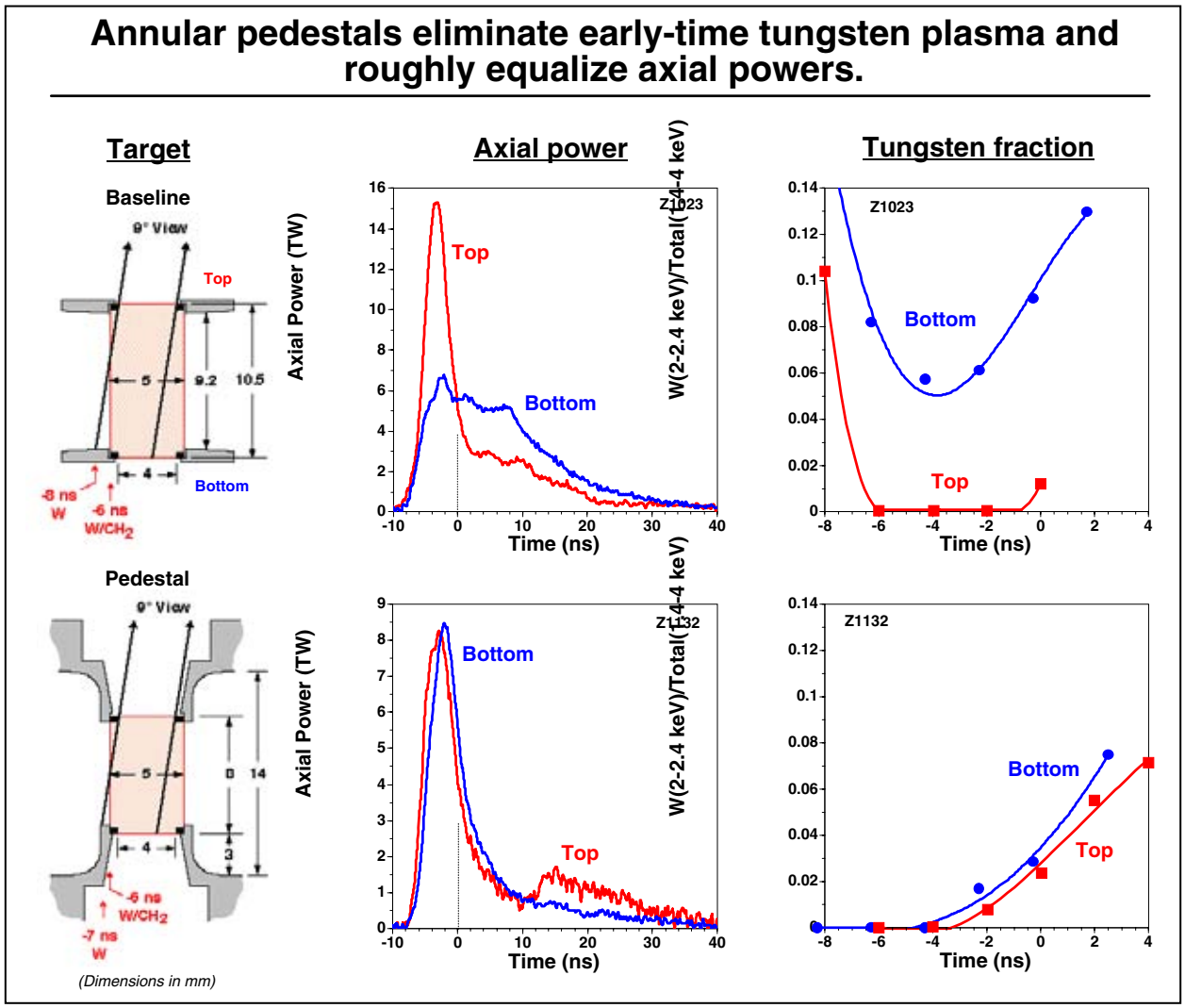

Figure 21. Pedestals eliminate up/down power asymmetry.

Results from the fixed implosion time scan of radius are shown in Figure 22. This scan was performed with a 14 mm long pinch and with 3 mm tall pedestals mounting the foam. Figure 22 plots the power radiated to the top and to the bottom on this scan for 4 values of the diameter of the outer wire-array. One sees from Figure 22 that the up/down power asymmetry is more extreme at the larger wire-array diameters. For the 32 mm case, inset D in Figure 22, the up/down power asymmetry appears to be eliminated. If it is desired to minimize up/down radiated power asymmetry a nested 32/16 mm diameter tungsten array appears to be better than a 40/20 mm nested tungsten wire array.

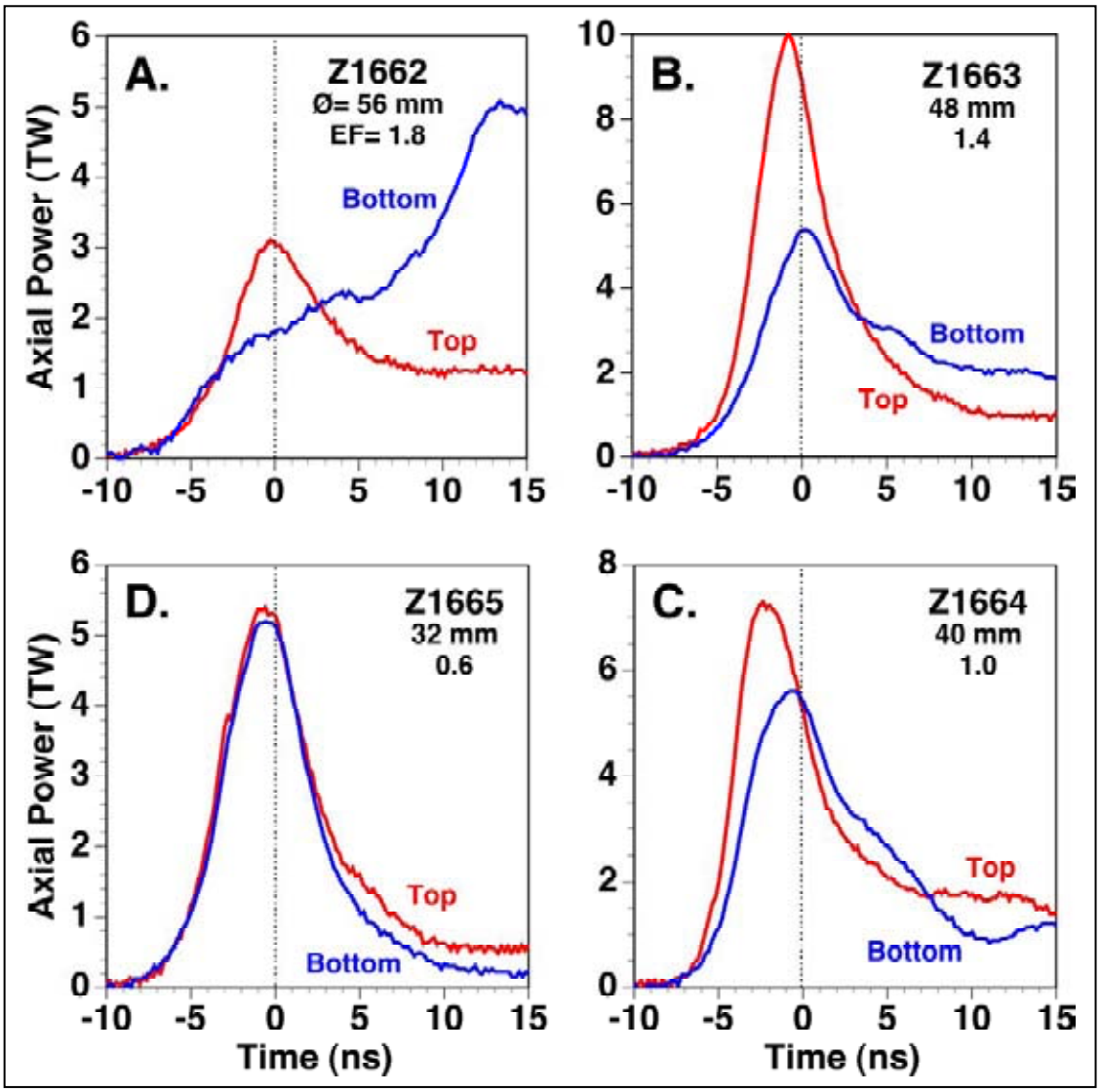

Figure 22. Up/down radiated power asymmetry as a function of outer array diameter in a fixed implosion time scan.

An explanation for the up/down power asymmetry that may explain the asymmetry in obscuring tungsten across the radiation exit apertures, lies in the relative magnitude of the radial electric field near the outer array wires during current initiation. [22] This radial electric field, E_r, is given by

$$E_r = UR/(2rN\Delta) \qquad (1)$$

where

U = voltage
R= array diameter
r= wire diameter

N= number of wires
Δ = anode cathode gap

In the fixed implosion time scan the radial electric field increases due to both the increasing array diameter and the decreasing wire diameter.

We show the results of the fixed implosion time radius scan along with simulated predictions in Figure 23. In this scan the up/down power asymmetry is eliminated at initial radii less than 32 mm. Also the predictions of the simulation deviate strongly from the measurements at initial radii less than 40 mm as will be discussed in the following section.

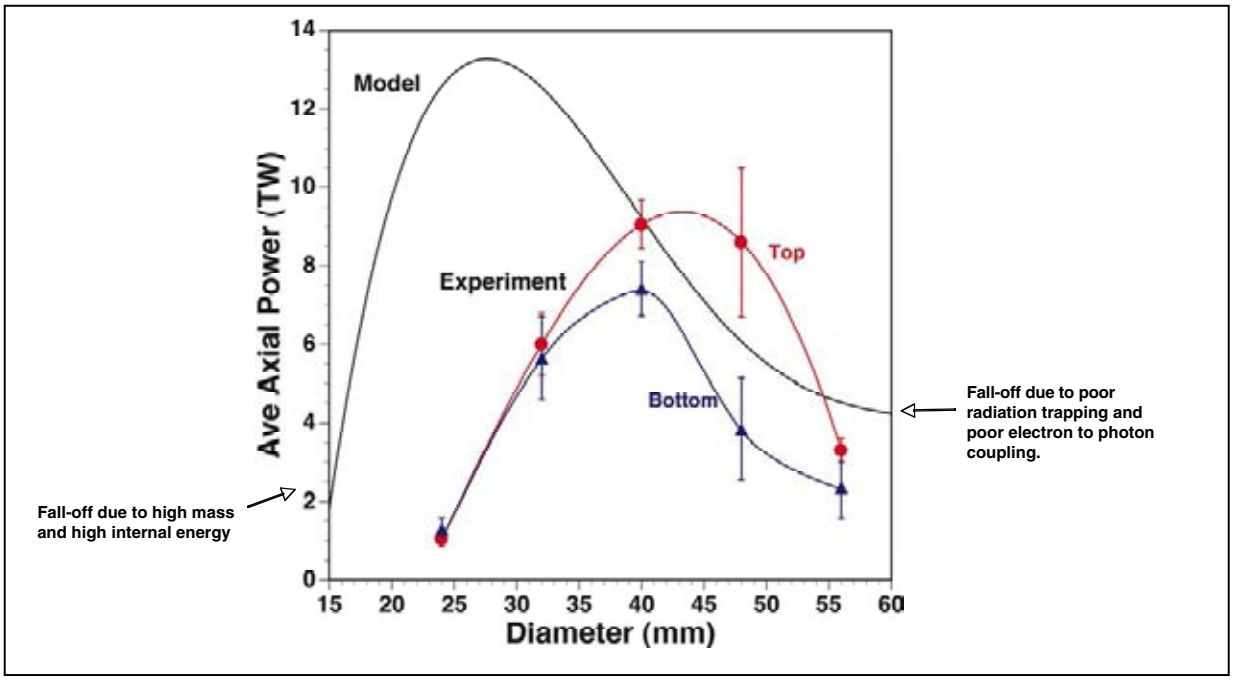

Figure 23. Power radiated to the top and bottom in a fixed implosion time radius scan along with predictions from simulation.

III. SIMULATION AND SCALING

We show the results for Z of 1D hydrodynamic simulations of the dynamic hohlraum along with experimental data points in Figure 24. The experimental data points, recorded at a variety of pinch lengths, have been scaled to a 1 cm long pinch. The power radiated axially is plotted as a function of the outer array diameter. The implosion time was kept constant by varying the product of the load mass times the square of the load radius. In these experiments the imploding wire-arrays were in a nested configuration with the inner nest being at one half the radius and one half the mass of the outer nest. The target foam on axis is 5 mm in diameter and its density is adjusted for its mass to match the sum of the masses of the nested wire-arrays. The simulations were run as an equivalent single shell system having the same mass and final kinetic energy as the nested arrays imploding onto the foam.

The simulated 1D implosions are far more stable that the actual implosions on Z, giving radiated powers with widths as sharp as 1 ns. To account for this discrepancy the simulated radiated powers have been averaged over 6 ns, roughly the fwhm of the experimentally measured axially radiated power.

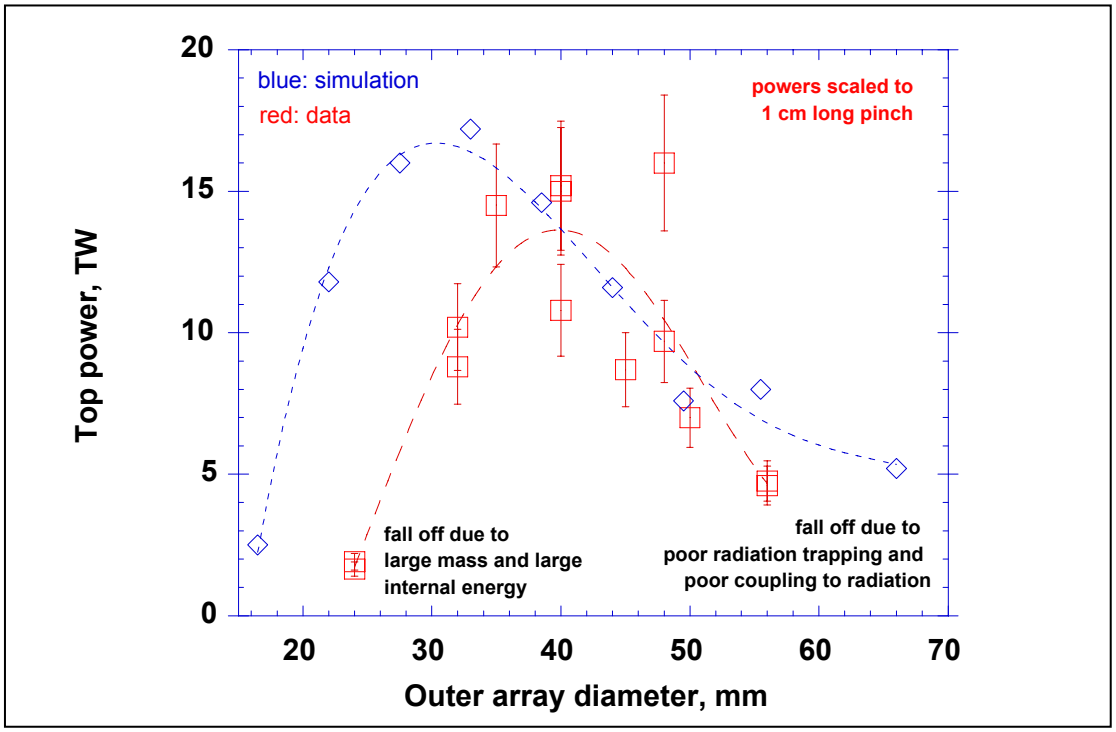

Figure 24. Top radiated power as a function of outer array diameter plotted along with results from 1D simulations.

The experimental data points have decent agreement with the simulations near the 40 mm diameter and show the fall off in radiated power at both large diameter and small diameter. However at small diameter the experimental data rolls over much sooner than the simulation. This is likely due to the simulation being more stable than the experimental implosion.

The simulation results indicate that the axially radiated power should have a fairly broad maximum over outer nest diameters between 28 and 40 mm. At diameters greater than 40 mm, the calculated 0D implosion velocity onto the foam exceeds 60 cm/μs. Subsequently the radiating shock wave in the foam, the dynamic hohlraum heating source, is also very fast, too fast for the electrons in the shock wave to couple efficiently to the radiation. As the diameter of the outer array is decreased below 40 mm the electrons and radiation in the shock wave couple efficiently and equilibrate. Also as the diameter is decreased the mass of the wire-arrays increases and the optical trapping of the wire-arrays increases which also increases the axially radiated power.

Below an outer array diameter of 28 mm the simulations show the axially radiated power falling. Below this diameter the 0D velocity of the imploding wire-arrays is less than 42 cm/μs. Below diameters of 28 mm the mass of the foam becomes a substantial energy sink, much of the kinetic energy of implosion is invested in internal energy of the foam, and the radiated power falls. Simulations indicate that the axially radiated power at small diameter may be recovered by reducing the foam mass.

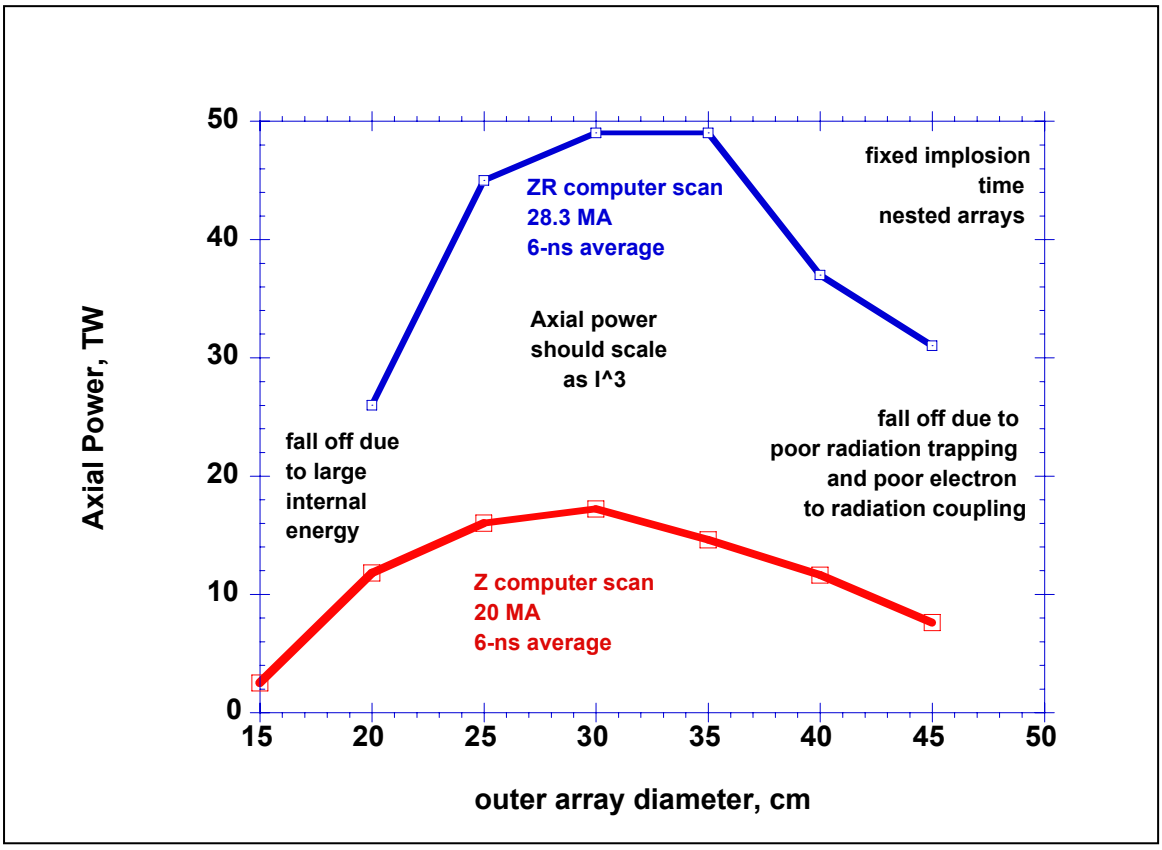

Figure 25. Results of simulations of axially radiated power versus outer array diameter for a fixed implosion time scan.

Simulations also show the axially radiated power scaling nearly as the cube of the current as shown in Figure 25. The simulations for ZR at 28 MA in Figure 25 were taken for a machine current rise time the same as Z at 90 ns.

The axially radiated power can scale more rapidly than the square of the current due to the effects of optical trapping. This can be shown analytically as follows.

If we assume the brightness of the radiating shock wave scales as the square of the current, the axially radiated power, P_a, is proportional to the square of the current times the optical depth, Γ, of the dynamic hohlraum wall. P_a is also proportional to the fourth power of the hohlraum radiation temperature, T. We then have

$$P_a \propto T^4 \propto I^2 \Gamma \qquad (2)$$

The optical depth is proportional to the wire-array mass to the power of 1.3 divided by the temperature to the power of 1.5. [23] Since the wire-array mass is proportional to the square of the current we have

$$\Gamma \propto I^{2.6} / T^{3/2} \qquad (3)$$

Combining the above two equations and solving for the temperature gives

$$T \propto I^{0.84} \qquad (4)$$

and

$$P_a \propto I^{3.36} \qquad (5)$$

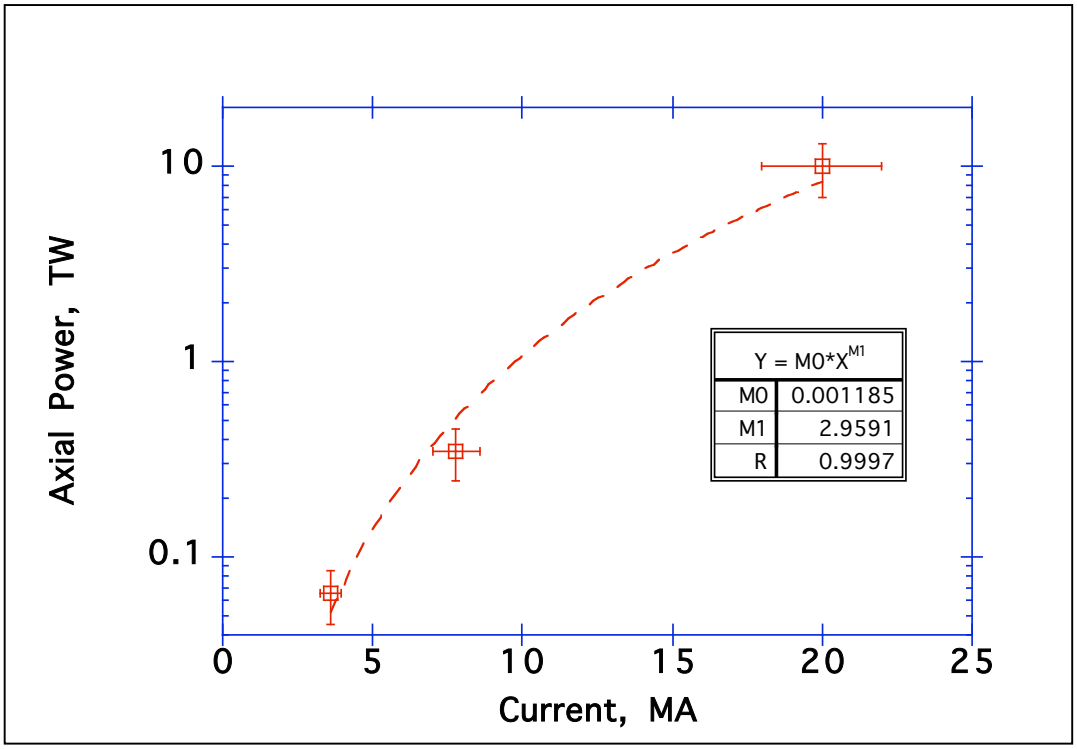

Figure 26. Experimental scaling of axially radiated power versus machine current.

In Figure 26 we show experimentally measured axially radiated powers for the 3 machines: ANGARA at 4 MA, SATURN at 7.5 MA, and Z at 20 MA. Although the machines have different implosion times and the dynamic hohlraum configuration is different in each case, the 0D impact velocity of the imploding shell onto foam in each case is nearly 60 cm/μs, and the final diameter of the stagnated dynamic hohlraum is in each case nearly 1 mm. These measurements indicate the axially radiated power to scale nearly as the cube of the current.

Projecting the scaling of Figure 26 to ZR at 28 MA would give an axially radiated power of 30 TW. Some caution must be taken with this projection as ZR is a longer implosion time machine than Z and pinch stability may be an issue in the scaling from Z to ZR. In scaling the dynamic hohlraum on SATURN at a 50 ns implosion time to Z at a 110 ns implosion time it was necessary to introduce the innovation of nested wire-arrays to recover on Z most of the stability exhibited by SATURN.

Because nested wire-arrays operate in a transparent mode, the scaling from Z at 110 ns implosions to ZR at 140 ns implosions may not be as detrimental as requiring stability for an extra 30 ns. If the stability is determined by the implosion time of the inner array once the current is switched to it, then the inner nest implosion time of 25 ns on Z must only scale to be stable up to an inner nest implosion time of 32 ns on ZR.

Results of 1D simulations of dynamic hohlraum loads on Z at a 105 ns implosion time and ZR with a 143 ns implosion time are shown in Figure 27. The axially radiated power in the case for Z has been smoothed over 7 ns to match the measured axially radiated power. For ZR we have smoothed the power over 9 ns in an effort to account for the longer implosion time on ZR. The simulations of Figure 27 again indicate that the axially radiated power should scale as the cube of the current.

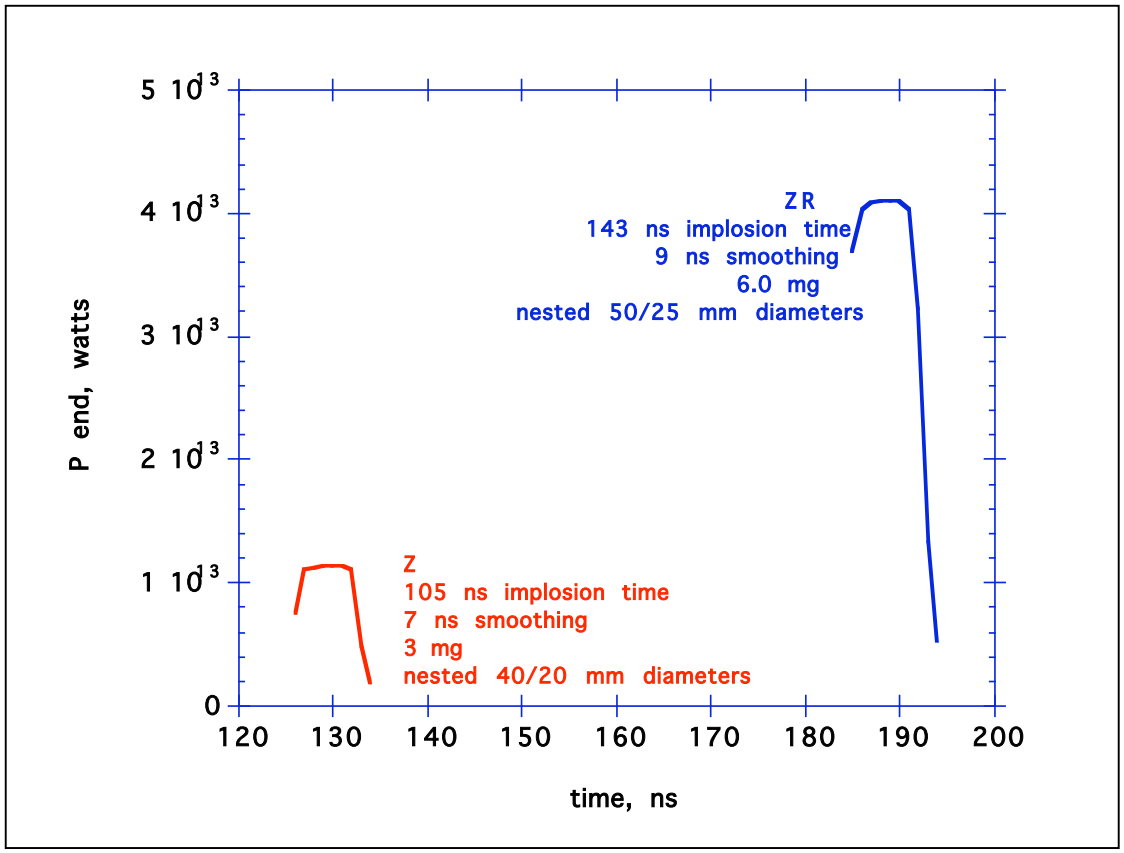

Figure 27. Results of simulations of axially radiated power for Z and ZR.

The 1D radiation hydrodynamic simulations of the dynamic hohlraum should only be used to provide insight into the dynamic hohlraum behavior and should not be used as an absolute design tool. The simulations give much sharper radiation power pulses than are measured. The experimental implosion proceeds with a variety of effects not included in the 1D simulations such as wire ablation, precursor plasma streaming in from wire coronas, and current switching to the inner wire array. Predictions by the 1D or 2D simulations in the mass scan and in the fixed implosion time scan to small radius have deviated considerably from the measured results. [19, 20] Predictions from the 1D simulations of the length scan were more accurate. [21]

IV. PROPOSED ZR DYNAMIC HOHLRAUM LOADS

The primary consideration in scaling the dynamic hohlraum load of Z to ZR is the considerably longer current pulse on ZR. The implosion time of the dynamic hohlraum on Z was 110 ns with a peak current of 21 MA. In order to increase the load current on ZR to over 28 MA the implosion time on ZR must approach 140 ns. Even longer implosion times on ZR should be explored as they can increase the ZR load current to over 30 MA.

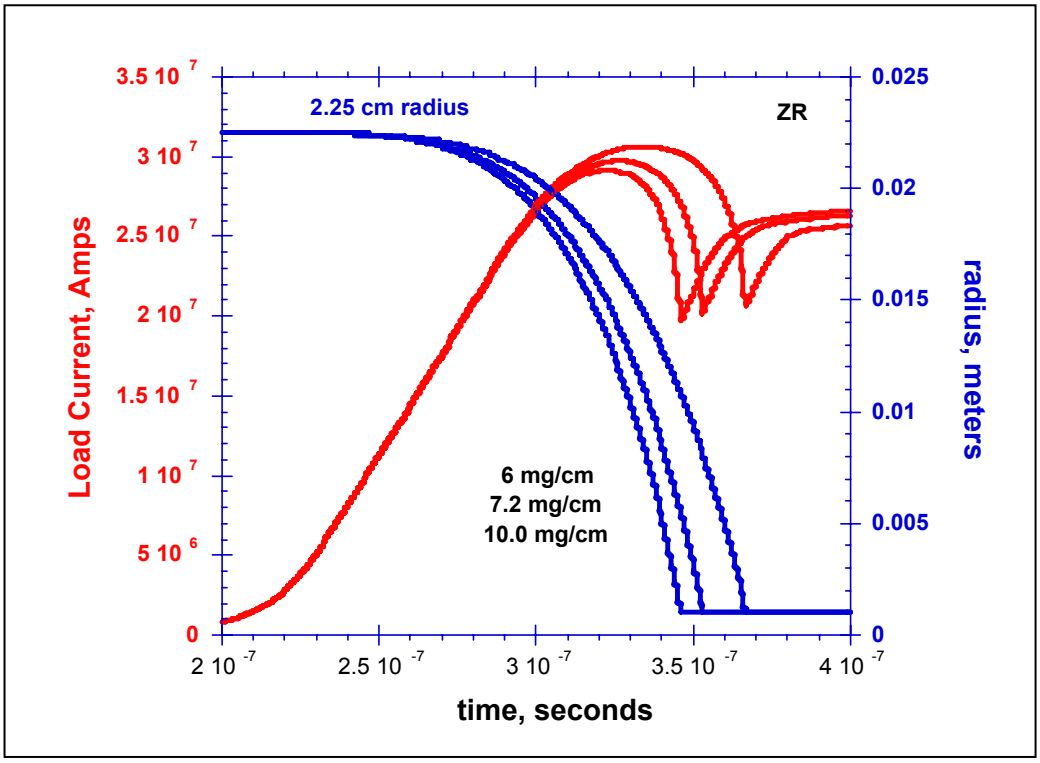

Figure 28. Results from 0D circuit simulations of implosions on ZR.

Since the implosion time on ZR will be longer than it was on Z, in order to maintain a 0D implosion velocity of 60 cm/μs, the array diameters on ZR must be increased with respect to Z by the ratio of the implosion times of ZR to Z. This was also the criterion in scaling from SATURN to Z.

These considerations for ZR are illustrated in Figure 28, the results of 0D circuit simulations of single shell implosions on ZR. The initial radius in these simulations is 2.25 cm. This single array radius has a similar final implosion velocity to a nested wire-array at radii of 2.5 and 1.25 cm. Figure 28 plots the load current and array radius versus time for 3 different mass loadings. Scaling the wire-array mass on Z, 3 mg, as the current squared, gives a 6 mg wire-array mass on ZR. In Figure 28 the 6 mg mass has the fastest implosion time but also the lowest load current. For this reason we consider it prudent to explore even larger mass loadings as they will experience larger peak load current. Note that this was not the case in the mass scan conducted on Z where the load current did not increase with increasing mass.

Shot	Wire Nos.	Diameters mm	Wire Diameter µm	Masses mg/cm	Foam density mg/cc	Foam mass mg/cm	length mm	wire gap µm	Implosion Time ns
1	340/170	50/25/6	8.9	4.0/2.0/6.0	21	6	10	462	143
2	332/166	45/22.5/6	10	4.9/2.45/6.0	21	6	10	426	143
3	324/162	40/20/6	11.18	6.0/3.0/6.0	21	6	10	388	143
4	332/166	50/25/6	10	4.9/2.45/6.0	21	6	10	451	154
5	324/162	50/25/6	11.18	6.0/3.0/6.0	21	6	10	485	168

Table 1. Recommended initial dynamic hohlraum loads for ZR.

A recommendation for initial dynamic hohlraum load configurations is given in table 1. To account for the longer implosion times on ZR we recommend baseline initial nested wire-array diameters as 50 and 25 mm, with 4 mg in the outer array and 2 mg in the inner array. We have also scaled the foam diameter up from 5 mm to 6 mm in proportion to the scaling of the array diameters. Keeping the foam mass matched to the tungsten mass gives a foam density of 21 mg/cc. The implosion time of the recommended baseline dynamic hohlraum load for ZR is 143 ns.

Since up/down asymmetry may persist at this baseline load, we recommend a fixed implosion time scan to smaller radii, increasing the tungsten mass to 7.35 and to 9 mg, but keeping the foam mass fixed at 6 mg. This scan to smaller radii may improve up/down power asymmetry as it did on Z. The 1D hydrodynamic simulations give guidance to not continue mass matching the foam to the tungsten at smaller diameters, as the foam can become a significant energy sink.

Finally we recommend increasing the mass of the tungsten while keeping the array diameters fixed at 50 and 25 mm. This mass scan may have better results than the mass scan performed on Z because the scan on ZR will lead to larger load current.

V. SUMMARY

We propose a baseline dynamic hohlraum load for ZR consisting of nested tungsten wire-arrays at 50 and 25 mm diameter, weighing 4 and 2 mg/cm that implode onto a 6 mm diameter foam target weighing 6 mg/cm. 0D circuit simulations of the implosion of this load show peak current reaching 28 MA and an implosion time of 143 ns. Measurements of axially radiated power on smaller machines indicate that the axially radiated power should scale as the cube of the current. This cubic current scaling is supported by analytic theory and by 1D simulations. If this scaling continues to hold true on ZR, despite the potential for instability growth at the longer implosion times of ZR, we may expect 30 TW of axially radiated power on ZR. We arrive at the proposed ZR load by simply scaling the mass as the current squared and the diameters as the ratio of the implosion times with respect to Z. The potentially more unstable longer implosion time of ZR with respect to Z may be mitigated by the beneficial effects of the transparency mode of the nested tungsten wires in which instability growth may be largely determined by the shorter implosion time of the inner nest. We expect that a smaller load on ZR consisting of nested tungsten wire arrays at 40 and 20 mm diameters weighing 6 and 3 mg will produce less or possibly eliminate up/down radiated power asymmetry. We recommend shooting the same 6 and 3 mg nested load at larger 50 and 25 mm diameters to access the larger peak current available on ZR at longer implosion times.

VI. REFERENCES

1. Spielman, RB, Long, F, Martin, T, et al., Proceedings of the 9th IEEE Pulsed Power Conference, Albuquerque, NM, edited by R. White and K. Prestwich (Institute of Electrical and Electronics Engineers, New York), p. 396, (1995)

2. Sanford, TWL, Mock, RC, Leeper, RJ, et al., Physics of Plasmas, **10**, No. 5, May, (2003)

3. Slutz, SA, Bailey, JE, Chandler, GA, et al., Physics of Plasmas, **10**, No. 5, 1875, May, (2003)

4. Bailey, JE, Chandler, GA, Slutz, SA, et al., Phys. Rev. Lett. , **89**, 95004, (2002)

5. Nash, TJ, Derzon, MS, Allshouse, G, et al., Proceedings of Fourth International Conference on Dense Z-Pinches 1997, pp. 175-182

6. Nash, TJ, Derzon, MS, Chandler, GA, et al., Physics of Plasmas, **6**, No. 5, Pt. 2, 2023-2029, May, (1999)

7. Smirnov, VP, Fast Liners for Inertial Fusion. Plasma Physics and Controlled Fusion, **33**, No. 13, pp. 1697-1714, (1191)

8. Peterson, DL, Bowers, RL, McLenithan, KD, et al., Physics of Plasmas, **5**, 3302, (1998)

9. Sanford, TWL, Allshouse, GO, Marder, BM, et al., Phys. Rev. Lett. **77**, 5063, (1996)

10. Deeney, CD, Douglas, MR, Spielman, RB, et al., Phys. Rev. Lett. **81**, No. 22, 4883-4887, November (1998)

11. Sanford, TWL, Lemke, RW, Mock, RC, et al., Physics of Plasmas, **9**, No. 8, 3573-3594, August (2002)

12. Lebedev, SV, Beg, FN, Bland, SN, et al., Physics of Plasmas, **8**, 3734 (2001)

13. Sanford, TWL, Cuneo, ME, Bliss, DE, et al., submitted to Physics of Plasmas, November 22, 2006

14. Nash, TJ, Chandler, GA, Leeper, RJ, et al., RSI, **74**, No. 3, 2211, March (2003)

15. Nash, TJ, Chandler, GA, Bailey, JE, et al., RSI, **77**, 10E319, October (2006)

16. Nash, TJ, Chandler, GA, Bailey, JE, et al., Proceedings of the Inertial Fusion Sciences and Applications Conference, Monterey, CA, edited by BA Hammel et al., p. 747, (2003)

17. Henke, BL, Yamada, HT, and Tanaka, TJ, RSI, **54**, No. 10, 1311, October (1983)

18. Nash, T.J., Sanford, TWL, Mock, RC, et al., JQSRT, **91**, No. 3, 333, March (2005)

19. Sanford, TWL, Nash, TJ, Mock, RC, et al., Physics of Plasmas, **12**, 022701, (2005)

20. Sanford, TWL, Lemke, RW, Mock, RC, and Peterson, DL, Physics of Plasmas, **10**, No. 8, 3252-3264, August (2003)

21. Sanford, TWL, Mock, RC, Slutz, SA, and Peterson, DL, Physics of Plasmas, **10**, No. 12, 4790-4799, December (2003)

22. Sanford, TWL, Jennings, CA, Rochau, GA, et al., Phys. Rev. Lett., **98**, 065003, (2007)

23. Lindl, J., Phys. Plasmas, **2**, No. 11, 3933, November, (1995)

DISTRIBUTION

20	MS1196	Tom Nash, 1677
100	MS1196	Tom Sanford, 1677
1	MS1196	Ray Mock, 1677
2	MS9018	Central Technical Files, 8944
2	MS0899	Technical Library, 4536